energies

MDPI

Article

Dynamic Modeling and Control Strategy Optimization of a Volkswagen Crafter Hybrid Electrified Powertrain

Aminu Babangida † and **Péter Tamás Szemes** *,†

Department of Vehicles Engineering, Vehicles and Mechatronics Institute, Faculty of Engineering, University of Debrecen, Ótemető u. 2-4, 4028 Debrecen, Hungary; aminu.babangida@eng.unideb.hu
* Correspondence: szemespeter@eng.unideb.hu
† These authors contributed equally to this work.

Abstract: This article studies the transformation and assembly process of the Volkswagen (VW) Crafter from conventional to hybrid vehicle of the department of vehicles engineering, University of Debrecen, and uses a computer-aided simulation (CAS) to design the vehicle based on the real measurement data (hardware-in-the-loop, HIL method) obtained from an online CAN bus data measurement platform using MATLAB/Simulink/Simscape and LabVIEW software. The conventional vehicle powered by a 6-speed manual transmission and a 4-stroke, 2.0 Turbocharged Direct Injection Common Rail (TDI CR) Diesel engine and the transformed hybrid electrified powertrain are designed to compare performance. A novel methodology is introduced using Netcan plus 110 devices for the CAN bus analysis of the vehicle's hybrid version. The acquired raw CAN data is analyzed using LabVIEW and decoded with the help of the database (DBC) file into physical values. A classical proportional integral derivative (PID) controller is utilized in the hybrid powertrain system to manage the vehicle consumption and CO_2 emissions. However, the intricate nonlinearities and other external environments could make its performance unsatisfactory. This study develops the energy management strategies (EMSs) on the basis of enhanced proportional integral derivative-based genetic algorithm (GA-PID), and compares with proportional integral-based particle swarm optimization (PSO-PI) and fractional order proportional integral derivative (FOPID) controllers, regulating the vehicle speed, allocating optimal torque and speed to the motor and engine and reducing the fuel and energy consumption and the CO_2 emissions. The integral time absolute error (ITAE) is proposed as a fitness function for the optimization. The GA-PID demonstrates superior performance, achieving energy efficiency of 90%, extending the battery pack range from 128.75 km to 185.3281 km and reducing the emissions to 74.79 gCO_2/km. It outperforms the PSO-PI and FOPID strategies by consuming less battery and motor energy and achieving higher system efficiency.

Keywords: DBC file; diesel engine; electrified powertrain; HIL; LabVIEW

check for updates

Citation: Babangida, A.; Szemes, P.T. Dynamic Modeling and Control Strategy Optimization of a Volkswagen Crafter Hybrid Electrified Powertrain. *Energies* **2024**, *17*, 4721. https://doi.org/10.3390/en17184721

Academic Editor: Adrian Ilinca

Received: 13 August 2024
Revised: 13 September 2024
Accepted: 19 September 2024
Published: 22 September 2024

1. Introduction

The conventional VW Crafter of the faculty of engineering operated only through the ICE and therefore consumed more fuel and caused dangerous gas emissions. The high dependence on diesel fuel and the devastating CO_2 emissions are undesirable. This research investigates the redesign of the vehicle into hybrid by cooperating a permanent magnet synchronous motor (PMSM) electrical machine with a 2011 Nissan Leaf battery pack. The diesel engine drives the front wheel, and the electric motor drives the rear wheel. However, the hybrid vehicle in this article operates in three modes: The first mode runs as a conventional vehicle operated through the diesel engine mode. The second mode is the electric mode, which a switching mechanism can activate. The third is the hybrid mode, which combines the engine and the electric modes. The transportation sector is the main source of carbon emissions which contribute about 25% of the CO_2 emissions [1] and has received serious attention worldwide [2]. As a result, nations worldwide are forced to decrease this negative trend [3], and have been committed to transforming the ICE vehicles into electric vehicles (EVs) [4,5], which support sustainable mobility [6]. The EVs have a limited operation range, higher energy costs, and longer charging times, limiting their adoption and practicality. Due to these retarding effects, hybrid electric vehicles (HEVs) have been adopted and became popular in the vehicle markets due to their low energy consumption [7] and have provided promising solution to mitigate energy crisis issues and environmental pollution [8]. Therefore, road transportation emissions have been eliminated, and the fuel consumption in conventional vehicles has been reduced with the development of the HEVs. In effect, the idea of HEVs has evolved to reduce air pollution levels and improve performance compared to ICE vehicles.

Fuel consumption and fuel economy are the critical indicators for the assessment of the performance of road vehicles. The fuel economy is characterized by the distance covered per unit of fuel, usually denoted as mile per gallon [MPG]. The MPG is a standard unit adopted in North America by the relevant stakeholders, including the consumers and the regulatory bodies. On the other hand, fuel consumption refers to the volume of the fuel consumed over a given distance covered. The fuel consumption is expressed in gallons per 100 kilometers [G/100 km] or liters per 100 kilometers [L/100 km] [9]. Therefore, fuel economy and fuel consumption are utilized to evaluate the efficiency of a vehicle. The growing adoption of HEVs worldwide has significantly improved the fuel economy and reduced consumption compared to ICE vehicles. Over the years, this has been achieved in HEVs through optimal operation of the ICE, aerodynamics improvement, regenerative braking, optimal motor control, idle-off technology, lightweight materials, smart charging of the vehicle, drive cycle optimization, and optimal vehicle speed control. These rapid advancements in HEV technology enable them to travel over an extended range of distances on a gallon of fuel, reducing fuel consumption and emissions. Consequently, this new development in HEVs has enabled cost savings over decades and reduced CO_2 emissions. Therefore, HEVs have been considered in the automotive industry and across scientific manuscripts as attractive and promising solutions for increasing global concerns about climate change and energy efficiency.

Ongoing research and development activities regarding energy management strategies in the context of scholarly discourse have continued to advance our knowledge in the field of EVs and HEVs technologies and have geared up innovative solutions in the automotive industry. Therefore, the increased demand for optimal performance and complexity of HEV powertrains have led to the development of advanced control techniques to optimize vehicle performance and reduce fuel consumption and carbon footprint. From the research perspective, many articles have been published base on the recent and cutting edge issues in the field of hybrid vehicles as in [10,11], which has led to advancements in control strategies and optimization methods. The function of the EMSs in HEVs is to allocate power demand to the vehicle's power sources efficiently. Research institutions have widely adopted EMSs for more than 20 years, and they are considered nonlinear and time-varying control problems [8]. Implementing these EMSs in HEVs has significantly improved fuel efficiency and reduced CO_2 emissions. These advancements have contributed to the widespread adoption of HEVs as a viable solution in transportation electrification compared to ICE vehicles. The EMSs have been adopted for efficient performance based on the durability of HEV components and optimal fuel consumption, and reducing emissions [12] . EMSs are generally classified into rule-based, optimization-based, and learning-based [8]. Rule-based facilitates integration in embedded controllers and presents excellent real-time performance. Rule-based EMSs are simple to implement [13], but requires human experience for better control effects. Optimization-based offers excellent performance but hinders implementation in real time. Learning-based offers outstanding potential for real-time implementation and provides a satisfactory control solution. However, it requires too much training time due to the large datasets, the training process is unstable, and there is difficulty in setting the objective functions [8]. Optimization-based EMSs have received wide attention in the context of scientific manuscripts. The commonly used optimization-base EMSs are the model predictive control (MPC), dynamic programming (DP), genetic algorithms (GA), particle swarm optimization (PSO), bacterial foraging optimization algorithm (BFOA), control theory [14], etc. For example PSO was proposed in [15] as EMS for multi-objective optimization for plug-in HEV, GA in [16], and adaptive dynamic programming (ADP) was proposed in [17] for a series-parallel HEV and a robust fuel economy was realized.

In recent years, nonlinear control algorithms have been the pioneering control philosophy utilized in electric vehicles for optimal fuel economy and reduced emissions. A nonlinear model predictive control (NMPC) was proposed in [18] and neural network (NN) in [19] for optimal fuel economy for plug-in HEV. In [20] NN was proposed for improving fuel economy in HEV. The NN has been a pioneering control strategy in the field of nonlinear control system like quadrotor [21] . In [22] an interval type-2 fuzzy Takagi-Sugeno-Kang (IT2TSK) was proposed to reduce the fuel usage in HEV. The proposed algorithm assessed on the basis of the engine and motor torques and the battery's SOC could save up to 19.03%, 12.54%, and 7.14%, respectively. The study in [23] proposed a deep learning (DL) algorithm for optimal fuel consumption in HEV. The suggested method is 12.2% and 6.4% better compared to rule-based and equivalent consumption minimization strategies. Predictive cruise control (PCC) was proposed in [24] for HEV based on the hierarchical control architecture to minimize fuel consumption. The study in [25] proposed two robust sliding mode controllers (SMCs) on a series HEV in order to optimize the system efficiency on the basis of speed and torque, respectively. The proposed controllers are promising and yield realistic performance for the HEV. A super-twisting sliding mode control (STSMC) was proposed in [26] to optimise the state of charge (SOC) in parallel HEVs to reduce fuel consumption and emissions. The simulation results demonstrated the STSMC algorithm as a promising and alternative control technique suitable for optimal fuel consumption in HEVs. In [27] a new offline-online hybrid deep reinforcement learning (DRL) strategy was proposed to improve the fuel economy in HEV. The simulation results demonstrated that the proposed approach is promising and relatively better than only the online learning algorithms. The study in [28] proposed adaptive neuro-fuzzy inference system (ANFIS) reduces fuel consumption in parallel HEV. Other control techniques, such as conventional proportional integral (PI), fuzzy PI, and rule-based were compared with the proposed controller, and the simulation results proved the proposed strategy's superiority. Most of the literature dedicated to investigating the theoretical implementation of the nonlinear control methods for hybrid vehicle applications. The neural network could be computationally intensive. The poor prediction in MPC makes the system performance worse and requires a precise system model. However, the adaptive controllers are excellent algorithms for nonlinear systems but can be sensitive to parameter tuning. According to the literature, optimization-based EMS approaches, such as GA, PSO, DP, and many more, were combined with control theory to realize effective control in HEVs.

Over the decades, the PID control algorithm has been widely adopted for industrial process control owing to its robustness and practicality for commercial mechatronics products. In contrast, most of the advanced controllers discussed earlier are often difficult to implement due to their complexity and lack of intuition for practical implementation, making PIDs suitable and alternative control candidates. The implemented vehicle controller in the hardware system in this research is a classical PID controller. However, linear controllers may not be suitable control candidates for EVs due to the system's complexity and intricate nonlinearities, which may compromise the system's stability. To mitigate this effect, an optimization method is combined with control theory for robust performance in order to achieve optimal fuel consumption, reduce CO_2 emissions, and extend the range of the battery pack in HEVs. GA is characterized by its global solid search [29], more straightforward implementation, robustness and ability to handle complex and multi-optimization problems effectively. Similarly, PSO has a fast convergence time [29], and requires less parameter tuning than GAs. Due to these advantages, these two optimization methods are commonly adopted to realize optimized system efficiency. The combined effect of these optimization techniques and control theory has yielded satisfactory performance in hybrid vehicles. Therefore, optimization methods have been used to search for an optimal performance in the field of vehicle engineering [30]. Nevertheless, the PID control algorithm has been optimized with PSO (PSO-PID), GA (GA-PID), grey wolf optimization (GWO-PID) and rule-based technique such as fuzzy logic (Fuzzy-PID) to realize robust performance. The study in [31] proposed a multi-operating point Fuzzy PID control strategy (MOPFPCS) and adaptive PSO-based fuzzy PID for the optimal fuel consumption in HEV. The two proposed methods have reduced fuel consumption by 18.3% and 15%, respectively. In recent years, nonlinear versions of PID such as fractional-order controllers (FOCs) in [32], sigmoid PID (SPID) in [33], neuroendocrine PID (NPID) in [34], nonlinear PID, adaptive PID, and many more have received extensive attention due to their robustness and ability to capture the nonlinear dynamic of complex system performance compared to integer-order controllers . Furthermore, the FOPID offers robust performance due to its ability to handle nonlinear systems compared to the classical PID integer order controller and can be more flexible and less complex compared to sigmoid and neuroendocrine PIDs. However, compared to integer order strategy, the tuning process in FOPID can be challenging due to higher number of tuning parameters. Apart from the more tuning parameters in SPID, its increased complexity due to the nonlinear function can be challenging. Moreover, higher number of tuning parameters makes the design and optimization of NPID often difficult.

The controllers mentioned above could be computationally intensive and, although robust, might not be realistic with our applications. Most of them require a precise system model and are sensitive to parameter tuning. The variants of the PIDs such as NPID and SPID have more tuning parameters than the standard PID of our reference vehicle, which could make the design and optimization difficult. Therefore, this article presents the design and control of the hybrid powertrain of the VW Crafter based on the online measurement CAN bus data, comparing the ICE and hybrid powertrain of the proposed vehicle. The research proposes GA-PID and compares with PSO-PI and FOPID control algorithms to reduce the proposed vehicle's fuel consumption and CO_2 emissions, justifying the effectiveness of the proposed controller. This article is an improved version of our paper submitted at the IEEE PEMC 2024 conference [35] .

However, this research reuses the existing experimental findings of our previous studies based on a new methodology for the vehicle monitoring system to give an in-depth analysis of the conventional and hybridized powertrain of the proposed vehicle. The primary contributions of this article are as follows:

- This article presents transforming a conventional VW Crafter into a hybrid vehicle, validating the power and torque requirements for the first time. A very few literature performed similar research.
- An enhanced GA-PID is proposed and comapred with PSO-PI and FOPID controls to optimize fuel consumption, reduce CO_2 emissions, and extend the 2011 Nissan Leaf battery pack range for the VW Crafter hybrid vehicle.
- This research adapted the experimental setup of our previous article for the electric mode from our previous study [35,36], which was obtained based on a novel data acquisition (DAQ) approach, enabling online CAN bus analysis for advancing the existing literature for optimizing the hybrid powertrain and proving the detailed analysis of the transformation process from the conventional to hybrid.
- This paper also presents a comprehensive performance comparison between the conventional and hybrid powertrains of the VW Crafter, providing valuable insights into the benefits and limitations of electrified hybrid powertrains.

The remaining part of this paper is arranged as follows: Section 2 presents the development workflow and the mathematical background descriptions of the vehicle systems. Section 3 presents the development of the control strategy and optimization. Section 4 presents the model development and simulation. Section 5 presents the experimental and simulation results. Section 6 presents a detailed discussion of the results. Finally, Section 7 presents the conclusions.

2. Materials and Methods

2.1. Development Workflow and Mathematical Description

To design the hybrid powertrain of the VW Crafter, we need to determine the force required to propel the vehicle. Subsequently, tractive power and torque are calculated. We can evaluate the traction motor and battery size based on the gear ratios and the final drive. A Tractive force is the net force required to propel the vehicle. According to Newton's second law of motion, the tractive force can be calculated by subtracting all the resistance forces acting in the opposite direction on the vehicle. This force calculation is done using the vehicle dynamics description. Vehicle dynamics, based on longitudinal dynamics, are characterized by the vehicle's motion, in which forward movement changes in response to the input from the driver or any other external conditions. Therefore, consider the free body diagram of the conventional Crafter with all the forces acting on the vehicle as shown in Figure 1. This mathematical description is used to estimate the torque and power requirement without taking into consideration the suspension components of the vehicle. However, the detailed vehicle dynamic description used has been adopted in this article as already described in our previous paper [36].

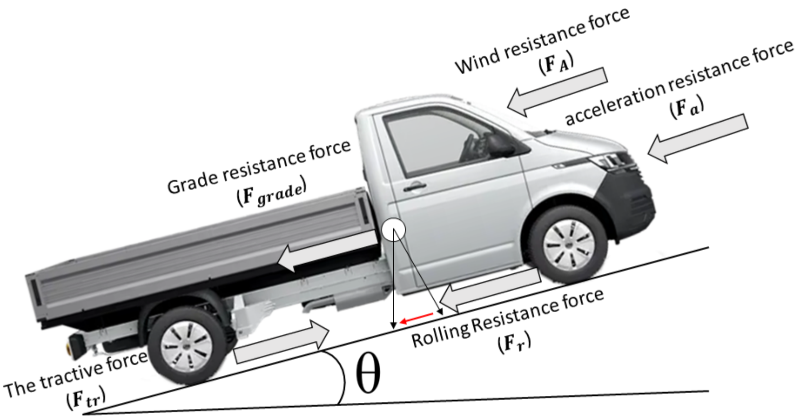

Figure 1. VW Vehicle Dynamics [35].

The tractive force, also known as tractive effort, is transmitted to the ground in order to propel the vehicle via the vehicle's driving wheels and axles. Suppose w is the vehicle weight in [kg] and is moving with speed v in meter/seconds [m/s or km/h] and moving against a slope of angle θ in [degree]. Therefore, the tractive force, in Newton [N] is required to overcome all the resistance forces, such as the wind, rolling resistance, grade, and acceleration forces in [N], respectively. The resistance force also known as the aerodynamic force is the force opposing the vehicle's motion as the vehicle travels in air. The rolling resistance force also known as drag force is the force due to the hysteresis losses on the vehicle's tire. The grade force is the force due to the gravity acting on the vehicle. Acceleration force is the inertial force acting on the vehicle during acceleration and braking. Therefore, according to the Newton's second law of motion of the classical mechanics as expressed in [35,37] can be described as follows:

$$\begin{cases} F_{tr} = F_A + F_r + F_{grade} + F_a \\ F_A = 0.5 \cdot \rho C_d \cdot A_F \cdot v^2 \\ F_r = w \cdot C_{rr} \cdot \cos\theta \\ F_{grade} = w \cdot \sin\theta \\ F_a = m_i \cdot a; \text{where}, m_i = 1.04 \cdot m \\ P = F \cdot v \\ E = P \cdot t \end{cases} \tag{1}$$

where F_{tr} is the tractive force [N], F_A is the wind resistance [N], F_r is the rolling resistance [N], F_{grade} is the grade resistance force [N], F_a is the acceleration resistance force [N], C_d is the coefficient of drag, A_F is the frontal area [m^2], v is the vehicle speed [m/s], C_{rr} is the coefficient of rolling resistance, θ is the angle of inclination [degree], m_i is the inertial mass, and m is the vehicle mass [kg], a is the vehicle acceleration [m/s^2], P is the tractive power [kW], E is the tractive energy [kWh], and t is the time period [seconds]. The tire radius can be calculated based on the information (205 × 75 R16) of the Crafter as follows:

$$\begin{cases} AR = \frac{h_s}{w_s} \cdot 100\% \\ r_t = r_m + h_s \end{cases} \quad (2)$$

where AR is the aspect ratio [%], h_s is the section height [m] (0.15375 m), w_s is the section width [m], and r_m is the rim radius [m] (0.2032 m). Based on the equations, the tire radius was calculated to be 0.357 m. Assuming the Crafter is a rear wheel drive when the electric mode is activated, the torque at the wheel of the vehicle is expressed as follows:

$$\begin{cases} F_{th} = \frac{i_x i_0 T_E \eta_P}{r_t} \\ F_{max} = \phi w \end{cases} \quad (3)$$

where F_{th} is theoretical tractive force [N], i_x is first gear ratio, i_0 is the final drive ratio, and T_E is the engine or motor torque [Nm], F_{max} is the maximum permissible tractive force of the VW Crafter [Nm], ϕ is the adhesion coefficient between the surface and the vehicle tire. Therefore, the theoretical tractive force was 17,001 N given the maximum torque of the engine as 340 Nm, when the first gear ratio is 5.06, η_P was taken as 90% for this design, and the final drive gear ratio is 3.92, respectively. Table 1 presents the general technical parameters of the VW Crafter. The tractive power and torque requirement has been analyzed in MATLAB software in order to validate the engine, motor, and battery size needed to design our reference vehicle. The curb weight, gross weight, and vehicle weight (2758 kg) after transforming the vehicle from the van to the pick-up style have been considered to accurately validate the torque and power requirement needed to propel it. Using the second part of the equation, the maximum permissible tractive force was 21,644.78 N which is greater than the calculated tractive force. This shows that there is a safe design because the vehicle would not slip.

Considering the VW Crafter, a total torque of 1118.384 Nm was obtained when activated in electric mode. The tractive power was 17.418 kW at the maximum allowable speed of 20 km/h when driving on electric mode. Therefore, the Parker electric PMSM motor with a maximum torque of 173 Nm was the right choice for this vehicle. Therefore, the maximum torque was approximately 7727.186 Nm when considering the engine or hybrid. This means that sufficient torque is provided by the engine and/or the electric motor to propel the vehicle even under a real-world driving cycle. Figure 2 shows the plot of the resistance forces acting on the VW Crafter, opposing the total tractive force. It can be seen that when the vehicle was subjected to a WLTP drive cycle at the speed of 0–131 km/h, the resistance forces such as the rolling resistance force, aerodynamic force, grade force, and acceleration resistance were 351.7 N, 989.9 N, 0 N, and 5020 N respectively. In this case, the total tractive force is the sum of these forces which was 6361.6 N. Figure 3 shows the tractive torque of 1930 Nm and a tractive force of 5407 N over the WLTP drive cycle at 1800 s. This shows that even over the WLTP drive cycle, the needed torque is much less than the maximum torque of 7727.186 Nm. Figure 4 shows the total tractive power which was obtained to be 79.85 kW over the entire WLTP drive cycle. In effect, the torque and power requirement for the VW Crafter is analyzed over the two different inputs: The constant speed of 20 km/h (max. allowable limit for electric mode only) and the real-world driving conditions (max. speed of 131 km/h). Therefore, if we consider the gear ratios of the vehicle, the maximum power and torque requirement of the engine and motor can be 103 kW, 340 Nm and 82.3 kW, 173 Nm, respectively. This is a safe design vehicle even when considering 30° sloping, which had a maximum tractive force of 16,613.61 N and the tractive torque of 5931.06 Nm, much less than the permissible value. Therefore, the vehicle model was considered under all the influence of the resistance forces and other factors such as slope, wind effect, and the tire-road contact conditions such as wet and dry asphalt, snow, and ice, to ensure safe design and the power and requirement of the vehicle under real driving conditions.

Table 1. VW Crafter Main Technical Specifications [35].

Parameter	Value	Symbol [Unit]
Length	5.986–7.319	l [m]
Width	2.040	w [m]
Height	2.355–2.798	h [m]
Curb Weight	2159–2196	W_c [kg]
Gross Weight	3500	W_g [kg]
Front Axle	1	T_F [m]
Rear Axle	1.346–1.901	T_R [m]
Tire Radius	0.357	r_t [m]
Centre of Gravity Height	0.785	CG [m]
Vehicle Front Area	4.05	A_F [m^2]
Rolling Resistance Coefficient	0.013	C_{rr} [-]
Drag Coefficient	0.3	C_d [-]
Air Density	1.225	ρ [kg/m^3]
Acceleration due to Gravity	9.81	g [m/s^2]
Engine Displacement	1968	D [cm^3]
Bore × Stroke	0.081 × 0.0955	BxS [m]
Number of Valves	16	v [-]
Compression Ratio	16.2:1	CR [-]
Engine Maximum Power	103	P_P [kW]
Gearbox	6-Speed, Manual	-

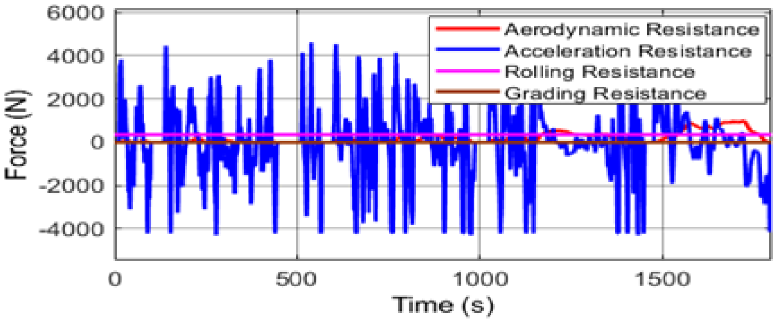

Figure 2. VW Crafter Resistance Forces.

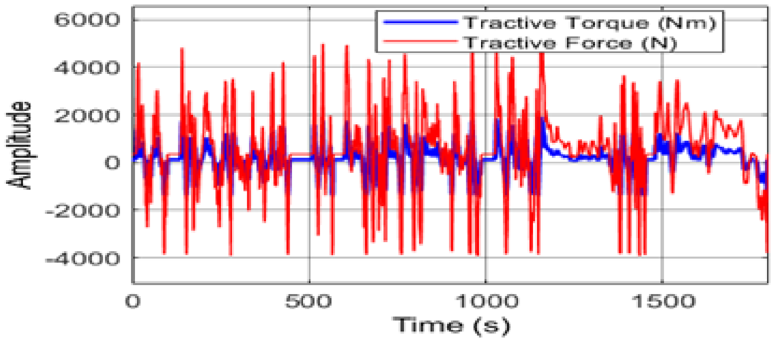

Figure 3. Total Tractive Force and Torque.

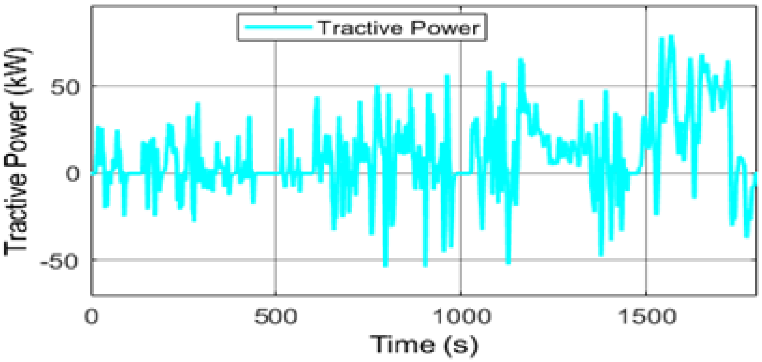

Figure 4. Total Tractive Power.

Figure 5 shows the development workflow for the VW Crafter hybrid vehicle design, highlighting the modeling process. The arrow does, however, does not present energy or power flow. The workflow comprises two primary steps: Step 1. The initial Design: In this design phase, the conventional VW Crafter model was created based on the previously discussed torque and power requirements. The results were then evaluated in order to establish a baseline for further design development. Step 2. Comprises the hybrid powertrain design: In this stage, the experimental data obtained through online CAN bus analysis was used for the design of the hybrid powertrain. Therefore, the model of the VW Crafter has been validated through the actual exprimental setup in the previous article [36]. This stage was built upon the insights gained from the initial design phase. The subsequent section elaborates on the actual assembly process of the vehicle. However, the enhanced PID controller was designed to optimize vehicle fuel consumption. The simulated and experimental results were compared and analyzed.

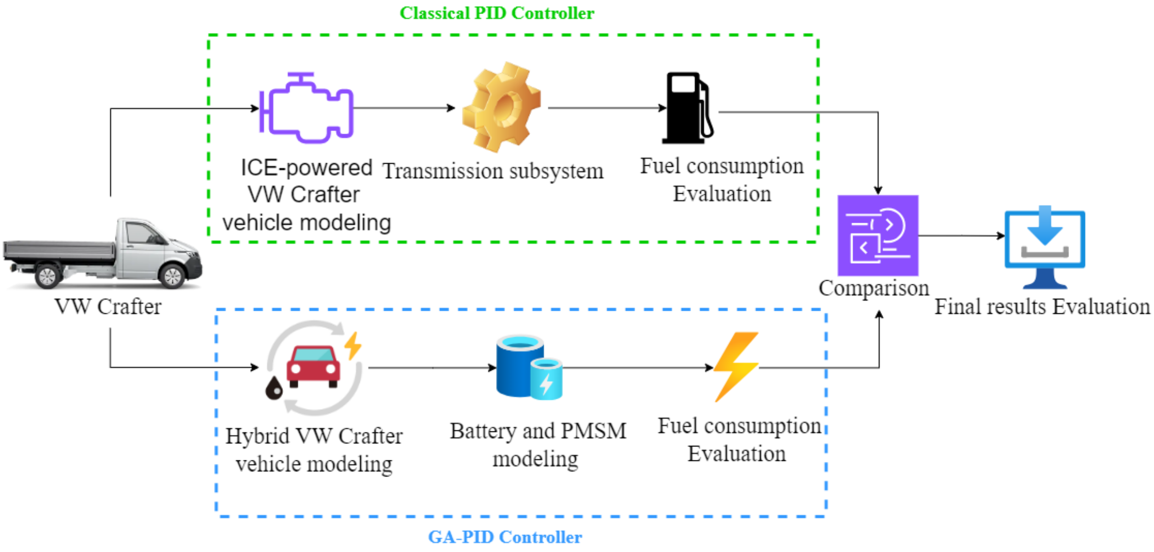

Figure 5. Development Workflow. This represents the development workflow of the modeling process involving the VW Crafter transformation from the conventional to hybrid electrified powertrain.

Figure 6 shows the general overview of the transformed hybrid vehicle with different subsystem models. It consists of the vehicle dynamics subsystem, motor subsystem, engine subsystem the controller, DC-DC converter, and the transmission subsystem. The DC-DC converter is not necessary for the motor at an abstraction level which can handle high voltage of the battery. The PID controller controls the vehicle speed and provides the optimal torque and speed needed propel the vehicle wheel. The engine is controlled in the engine management to provide optimal torque which is combined with the motor torque to be translated into vehicle movement.

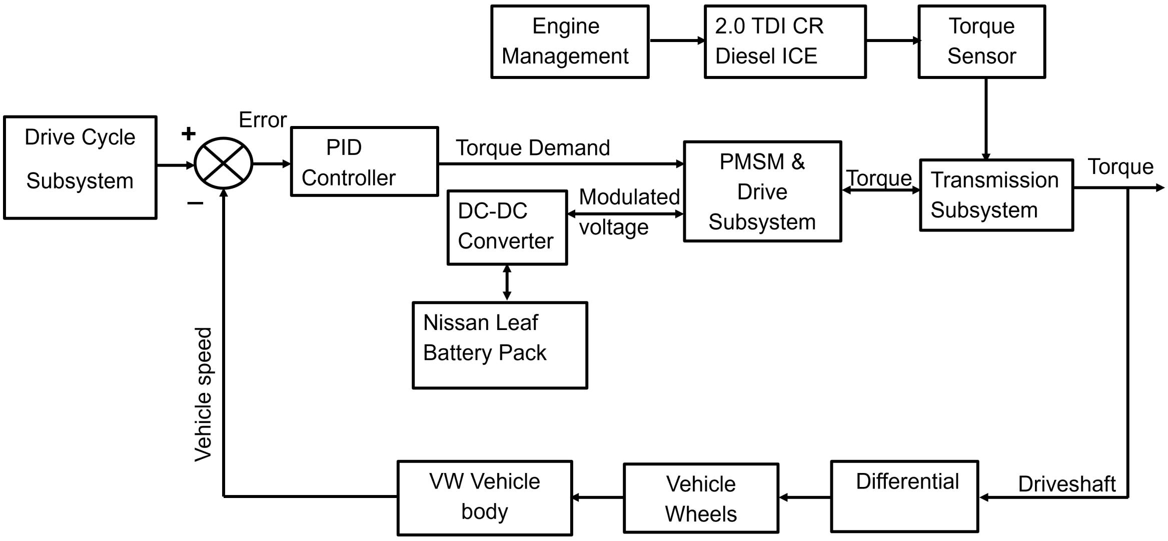

Figure 6. VW Crafter Closed-Loop Overview. This represents the overall overview of the subsystems of the hybrid vehicle model described in this section.

2.2. Nissan Leaf Battery Modeling

In this article, a 2011 Nissan Leaf battery pack based on lithium-ion batteries (LIBs), commonly used in EVs and HEVs, is utilized as proposed in our previous studies. The LIBs have gained significant research attention in recent years and have become the preferred choice for EVs, both currently and in future research, due to their exceptionally high energy and power density features [38]. Therefore, the superiority of LIBs in this regard makes them a suitable candidate in the field of electric vehicles, driving the widespread adoption of LIBs in the automotive industry. The 2011 Nissan Leaf battery pack comprises 48 modules, and in each module, there are four cells, each containing four cells arranged in two series pairs in parallel, totalling 192 cells in the pack. The battery pack has a 24 kWh rated energy capacity and a nominal voltage of 360 V. Moreover, the individual cell specifications include a nominal voltage of 3.75 V, maximum voltage of 4.2 V, discharge voltage of 2.5 V, and current capacity of 33.1 Ah. The pack achieves a maximum voltage of 403.2 V, a current capacity of 66.2 Ah, and a power output exceeding 90 kW [39].

To develop a model of the Nissan Leaf battery, it is assumed to be a spontaneous electrochemical redox reaction that does electrical work, converting chemical energy into electromotive force (EMF). This perspective enables us to model the Nissan Leaf battery as an energy conversion system. By applying fundamental principles of electrochemistry and thermodynamics, we derive a mathematical model that captures the dynamic behavior of the battery, including its voltage, current, and state of charge (SOC) as expressed in [39] as follows:

$$\begin{cases} V_r^0 = -\frac{\Delta G^0}{nF} \\ V_b = V_r^0 - \frac{RT}{nF} log_e Q_R - \Omega_d \\ V_b = V_r^0 - \frac{RT}{nF} log_e Q_R - R_b I_b ; \Omega_d = R_b I_b \end{cases} \tag{4}$$

where R is the ideal gas constant [J/K/mol], ${V_r}^0$ is the cell voltage [V] (no-load open circuit), is the ohmic drop Ω_d, ΔG^0 is the change in the Gibbs free energy [J/mol], n is the number of moles of electron transferred according balanced equation of the redox reaction [39], F is the Faraday's constant (96,485 J/V-mol), Q_R is the reaction quotient, R_b is the cell resistance [Ω], I_b is the cell current [A], and V_b is the cell voltage [V], T is the temperature [K]. The battery cell voltage can be expressed as:

$$V_b(I_b, y) = {V_r}^0 - A log_e(B \cdot y) - K \cdot y - F e^{G(y - y_3)} - R_b I_b \tag{5}$$

where y is a function of the battery depth of discharge (DOD), the battery SOC, and the capacity. In addition, y_3 is the value when the exponential drop starts, A, B, K, F, and G are the constants [39]. Equation (5) can be expressed as a function of the DOD as follows:

$$\begin{cases} V_b(I_b, DOD) = V_r{}^0 - Alog_e(B \cdot DOD) - K \cdot DOD - Fe^{G(DOD-DOD_3)} - R_b I_b \\ V_b(I_b, DOD) = V_b(nl)(DOD) - R_b I_b \\ V_b(nl)(DOD) = V_r{}^0 - Alog_e(B \cdot DOD) - K \cdot DOD - Fe^{G(DOD-DOD_3)} \end{cases} \tag{6}$$

Therefore, these equations is presented by the general equivalent circuit consisting of the voltage source in series with the resistance as studied in [39]. To obtain the model of the whole pack, we connect the 48 modules in series and determined the pack parameters if I_b and V_b are the cell current and voltage, based on the following formulations, respectively:

$$\begin{cases} V_{bp} = 2 \cdot N_m V_b \\ I_{bp} = 2 \cdot I_b \\ R_{bp} = N_m R_b \\ C_b = N_c V_b I_b \\ C_r = \frac{C_{re} \cdot C_I}{C_{Ah}} \end{cases} \tag{7}$$

where N_m is the pack modules, V_{bp} is the battery pack voltage [V], $I_b p$ is the battery pack current [A], R_{bp} is the battery pack resistance [Ω], C_b the capacity of the pack [kWh], C_r is the remaining capacity of the battery pack [kWh],N_c is total cells in the pack, C_{re} is the residual capacity [Ah], C_I is the initial energy capacity [kWh], and C_{Ah} is the total the current capacity [Ah]. Based on this, the entire pack can be represent using the circuit diagram in Figure 7. Table 2 presents the parameters of the 2011 Nissan Leaf battery pack. The pack comprises 48 modules, cabling, circuitry, and interconnects, providing a robust chassis to protect the battery cells. The total weight of the battery pack is 293.9 kg, with an energy density of 81.65 Wh/kg. The rated capacity of each cell is 33.1 Ah at a 0.3 C-rate for 3 h, which means 155.194 Wh per cell or 66.2 Ah (24 kWh) per pack. This implies that the cell or pack will deliver the rated capacity when discharged at a 0.3 C rate (9.93 A per cell or 19.86 A per pack) for 3 h. The 0.3 C rating typically approximates the discharge current under normal driving conditions. However, depending on the application and current requirements, different C ratings may be specified. This flexibility allows for tailored performance to meet specific applications. In our case, the C-rating is within the range of 2 C–5 C.

Table 2. The General Nissan Leaf Battery Specification.

Parameter	Cell	Module	Pack
Number of Cells	1	4	192
Voltage [V]	3.75	7.5	360
Current Capacity [Ah]	33.1	66.2	66.2
Energy Capacity [kWh]	0.124	0.4965	24
Volume [L]	0.445	2.365	494.2
Weight [kg]	0.799	3.8	293.9
Energy Density [Wh/kg]	155.194	130.66	81.65
Energy Density [kWh/kg]	0.155	0.131	0.08165

The DOD is the percentage of the Nissan Leaf battery discharged. The DOD is 100 minus the SOC in percent. However, if our battery has 67% DOD, 24 kWh rating, this implies that the discharge of the battery cannot exceed 16.08 kWh. C-rating is one of the crucial features of the battery to take into consideration when purchasing it. It is used to label the battery's current capacity. For example, a 30 Ah fully charged battery with a 1 C rating gives a current of 30 A in one hour. If the same battery is discharged at a C rating of 0.5 C, it delivers a current of 15 A in 2 h. If it is discharged at 2 C, it gives a current of 60 A for 30 min.

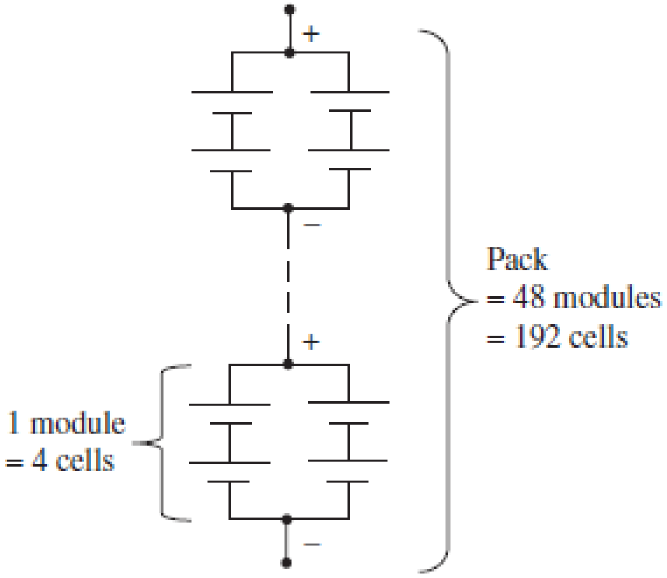

Figure 7. Battery Equivalent Model [39].

Figure 8 shows the MATLAB model of the whole battery pack consisting of the 48 modules and in each module. Meanwhile, Figure 9 illustrates the characteristics of each cell when discharging at 0.3 C, with a current of 9.93 A. As shown in Figure 9, the maximum charging voltage for each cell is 4.2 V, and the recommended discharge voltage is 2.5 V, while for the entire pack, the maximum voltage is 403.2 V and 250 V, the discharge voltage. This demonstrates that the battery can perform effectively at the specified C-rating, providing 9.93 A per cell or 19.86 A for the entire pack. This proves that the battery can meet the required specifications and function reliably under the recommended operating conditions. However, due to the complexity of the whole battery and the nonlinear dynamics of the HEV system, and to speed up the simulation, the battery pack has been represented by a compressed battery pack in the form of the system-level model.

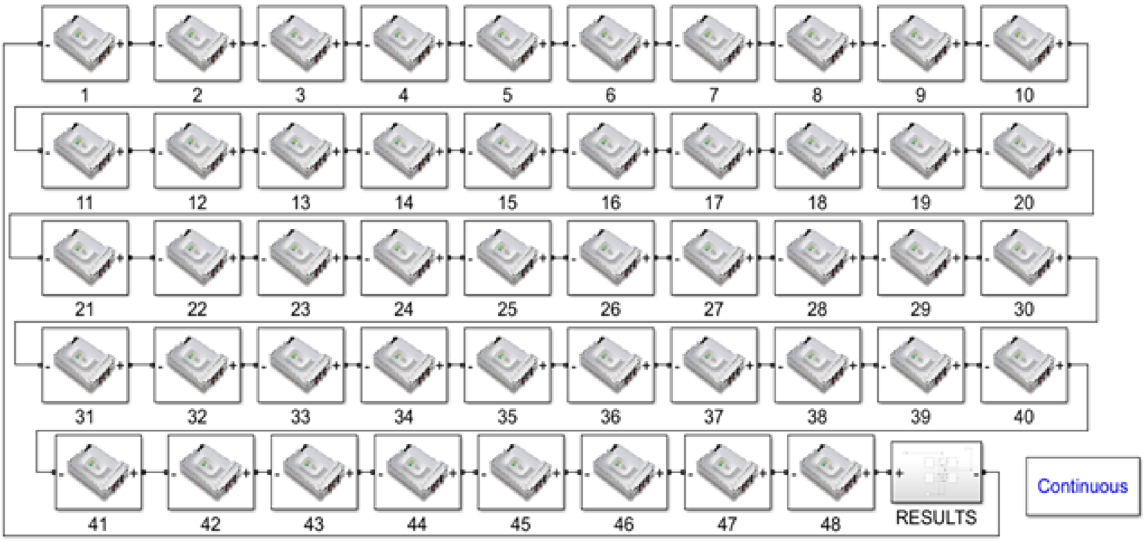

Figure 8. MATLAB Model of the Nissan Battery Pack.

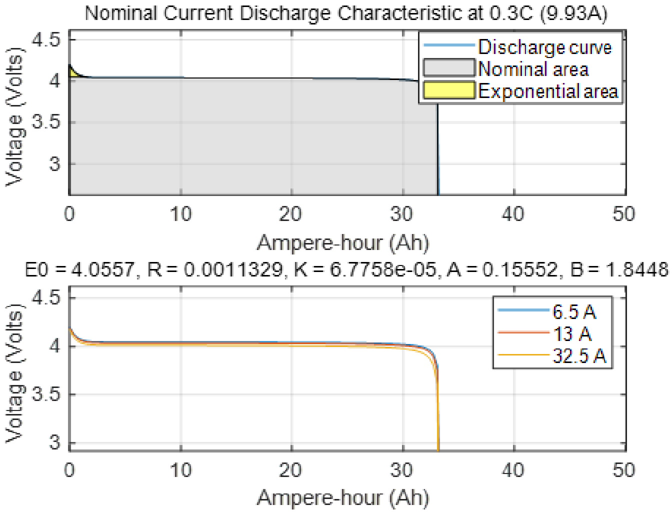

Figure 9. Battery Discharge Characteristics.

2.3. ICE Dynamic Modeling

In this article, the engine is modeled based on the generic model in Simscape and the other mathematical formulations have been adapted from [40]. Therefore, the ICE model is parameterized on the basis of a third-order polynomial as expressed in [41] as follows:

$$\begin{cases} \omega_N(\omega) \equiv \frac{\omega}{\omega_{PP}} \\ P(\omega(\omega_N)) = P_P p_N(\omega_N) \\ p_N(\omega_N) = s_1\omega_N + s_2\omega_N^2 + s_3\omega_N^3 \end{cases} \tag{8}$$

where $\omega_N(\omega)$, ω, and ω_{PP}, are the normalized ICE speed, current ICE speed [rpm], and ICE speed [rpm] at the peak power. Moreover, $P(\omega(\omega_N))$, P_P, and p_N are the current ICE power [kW], peak ICE power [kW], and normalized ICE power. Finally, s_1, s_2, and s_3 are the constant coefficients of the polynomial [41]. For wide open throttle condition, the ICE torque is expressed as follows:

$$\begin{cases} T(\omega(\omega_N)) = p_1 + p_2\omega_N + p_3\omega_N^2 \\ p_1 \equiv \frac{s_1 P_P}{\omega_{PP}} \\ p_2 \equiv \frac{s_2 P_P}{\omega_{PP}} \\ p_3 \equiv \frac{s_3 P_P}{\omega_{PP}} \\ \omega_{NPP} = \omega_N(\omega_{NPP}) = 1 \end{cases} \tag{9}$$

where ω_{NPP} is the normalized engine speed aligned with peak power. If we substitute the normalized engine speed (ω_{NPT}) at peak power (P_P) [kW] into p_N and set $p_N((\omega_{PP}))$ to zero, we have:

$$\begin{cases} s_1 + s_2 + s_3 = 1 \\ s_1 + 2s_2 + 3s_3 = 0; p_N = 0 \\ \omega_{NPT} = \omega_N(\omega_{PT}) = \frac{\omega_{PT}}{\omega_{PP}} < 1 \end{cases} \tag{10}$$

where speed of the peak power is greater than the speed of the peak torque. Based on the polynomial formula, we can find the normalized, dimensionless torque (τ_N) and set the slope to zero and solve for s_i [41]:

$$\begin{cases} \frac{d\tau_N(\omega_{NPT})}{d\omega} = s_2 + 2s_3\omega_{NPT} = 0 \\ s_1 = \frac{3-4\omega_{NPT}}{2(1-\omega_{NPT})} \\ s_2 = -\frac{\omega_{NPT}}{(\omega_{NPT}-1)} \\ s_3 = \frac{1}{2(\omega_{NPT}-1)} \end{cases} \tag{11}$$

Therefore, the engine torque $T(\omega(\omega_N))$, the peak torque (T_P), normalized engine speed at peak torque (ω_{NPT}), engine speed at peak power (ω_{PP}), and engine speed at peak torque (ω_{PT}) are related as follows [41]:

$$\begin{cases} T(\omega(\omega_N)) = \frac{2T_P}{3-\omega_{NPT}}(s_1 + s_2\omega_N + s_3\omega_N^2) \\ 2T_P\omega_{PP}^2 - 3P_P\omega_{PP} + P_P\omega_{PT} \\ \omega_{PP} = \frac{3P_P + \sqrt{P_P(9P_P - 8T_P\omega_{PT})}}{4T_P} > \omega_{PT} \end{cases} \tag{12}$$

where ($T_P\omega_{PT}$) is equivalent to power at peak torque (P_{PT}), which is always less than peak power (P_P) [41].

For the partially opened throttle condition, the following equation can be described:

$$\begin{cases} \Pi = max(\Pi_i, \Pi_c) \\ \frac{d\Pi_c}{dx} = \frac{0.5(1-\tanh(4\frac{\omega-\omega_r}{\omega_t}))-\Pi_c}{\tau} \end{cases} \tag{13}$$

where Π is the throttle [%], Π_i is the input throttle [%], Π_c is the controller throttle, ω is the engine speed [rpm], ω_r is the partial or idle speed reference [rpm], ω_t is the controller speed threshold [rpm], and τ is the controller time constant [seconds] [41]. To compute the other parameters in this research, such as the engine efficiency, fuel flow rate, etc., we adapted the formulations described in [40], and as adapted for our previous paper [36]. Therefore, the ICE torque $T(\omega(\omega))$ [Nm] is linked to the engine power ($P(\omega(\omega_N))$) [kW], and the rotational speed ω [rpm].

$$\begin{cases} T(\omega(\omega_N)) = \frac{P(\omega(\omega_N))}{\omega} \\ \eta_f = \frac{1}{Q_{hv}SFC} \\ SFC = \frac{m_f}{P(\omega(\omega_N))} \\ MEP = \frac{P(\omega(\omega_N))n_R}{V_d N} \\ MEP = \eta_f \eta_v Q_{hv} P_{ai}\frac{F}{A} \\ \eta_v = \frac{m_a}{P_{ai}V_d} \end{cases} \tag{14}$$

where η_f is the ICE efficiency [%], Q_{hv} is the heating value [J/kg], SFC is the specific fuel consumption [g/kWh], m_f is the fuel flow rate [g/s], n_R is the number of crank revolutions for each power stroke per cylinder [rev/power str/cyl] (dimensionless), V_d is the volume displaced [L], N is the number of revolutions of the crankshaft [rpm], MEP is the mean effective pressure [pa], η_v is the volumetric efficiency [%] , P_{ai} is the air-inlet density [kg/m^3], $\frac{F}{A}$ is the air-fuel ratio, and m_a is the air mass [kg]. It should be noted that all the units were appropriately converted based on the conversion factor to get the required quantity in the stated unit in this research, for example, to get unit in hour should divide by 3600, or divide by 1000 to get unit in kg, and so'on. However, MATLAB software takes care of all the conversions to the stated units utilized throughout this research. Table 3 presents the technical specification of the ICE used in this research.

Table 3. The ICE Technical Specifications [35].

Parameter	Value	Symbol [Unit]
Number of Cylinders	4, Inline	-
Fuel Type	Diesel	-
Fuel System	Common Rail (CR)	-
Fuel Density	820–845	ρ_F [g/L]
Engine Displacement	1986	D [cm^3]
Bore × Stroke	0.081 × 0.0955	BxS [m]
Number of Valves	16	-
Compression Ratio	16.2:1	-
Engine Maximum Power	103	P_P [kW]
Engine Maximum Torque	340	T_P [Nm]
Number of Valves	16	v [-]
Gearbox	6-Speed, Manual	-
After Treatment Systems	Diesel Particulate Filter	-
Engine Time Constant	0.4	τ [s]

Engine Mode Gearbox Design and Gearshift

The transmission system in this research requires the driver to manually select the gears by operating the gearshift and the clutch. The traditional VW crafter modeled is powered by the four-cylinder, four-stroke, 2.0 L volume ICE diesel engine. The throttle set-point was determined by a proportional integral controller based on the WLTP profile. The vehicle is coupled by a 6-speed manual gearbox engaged and disengaged by a friction disc clutch to facilitate movement. A shift logic gearbox controller is developed to control the gearshifting strategy. The clutch selection for each gear is presented in Table 4, from the first gear to the final gear drive. Vehicle speed and torque are the common parameters used to initiate gearshifts [42]. Theoretically, the gearshifting strategy can be expressed as in [43] as follows:

$$\begin{cases} R_{firstest.} = \frac{r_w m}{T_{eng.}\eta_f}\left(a_{WLTP} + g\sin\theta_{max}\right) \\ v = \frac{1000\pi r_w}{30 R_{firstest.}} \\ R_{first} = \frac{r_w}{T_{eng.}\eta_f}\left[a\left(m + \frac{I_{Eff}}{r_w^2} + F_A + F_r + F_{grade}\right)\right] \\ R_{top} = \frac{2\pi r_w N_{engmax.}\eta_f}{60 v_{motorway}} \end{cases} \tag{15}$$

where R_{first} is the first gear ratio, $R_{firstest.}$ is the estimated gear ratio, v is the vehicle speed [km/h], which is calculated at 1000 rpm speed of the engine, a is the vehicle's acceleration [m/s^2], m is the vehicle mass [kg], $T_{eng.}$ is the torque of the engine [Nm], r_w is the tire radius [m], I_{Eff} is the inertia effect [kgm^2], R_{top} is the top gear ratio, $N_{engmax.}$ is the maximum speed of the engine [rpm], and $v_{motorway}$ is the maximum motorway vehicle's legal speed [km/h]. Equation (15) is used to optimize the gear ratios until the correct gear ratio achieved. Therefore, in this research we adapted the same gear ratio from the manufacturer to ease our design.

Table 4. Clutch Schedule and Six-Speed Manual Gearbox [35].

Gearshift	Gear Ratio	A	B	C	D	E	F
1st	5.06	1	0	0	0	0	0
2nd	2.61	0	1	0	0	0	0
3rd	1.52	0	0	1	0	0	0
4th	1.00	0	0	0	1	0	0
5th	0.79	0	0	0	0	1	0
6th	0.68	0	0	0	0	0	1
Final	3.92	1	1	1	1	1	1

2.4. PMSM Dynamic Modeling

The three-phase supply voltages and currents are related as expressed in [35,44] as follows:

$$\begin{cases} V_A = \frac{d}{dt}\Psi_A + I_A R_s \\ V_B = \frac{d}{dt}\Psi_B + I_B R_s \\ V_C = \frac{d}{dt}\Psi_C + I_C R_s \end{cases} \tag{16}$$

where Ψ_A, Ψ_B, Ψ_C are the flux linkages [Weber], I_A, I_B, I_C are the phase currents [A], R_s is the phase resistance [Ω]. If L_s is the phase inductance [H], the rotor coupling flux linkage is expressed as in [44] as:

$$\begin{cases} \Psi_A = L_s I_A + \Psi_r \cos\theta \\ \Psi_B = L_s I_B + \Psi_r \cos(\theta - \frac{2\pi}{3}) \\ \Psi_C = L_s I_C + \Psi_r \cos(\theta + \frac{2\pi}{3}) \end{cases} \tag{17}$$

However, using the d_q reference frame, the model of the PMSM can be represented in d_q rotating reference frame:

$$\begin{cases} V_q = R_s I_q + \omega_r \lambda_d + \frac{d}{dt}\lambda_q \\ V_d = R_s I_d - \omega_r \lambda_q + \frac{d}{dt}\lambda_d \end{cases} \tag{18}$$

where:

$$\begin{cases} \lambda_q = L_q I_q \\ \lambda_d = L_d I_d + \lambda_r \end{cases} \tag{19}$$

Therefore, Equation (18) becomes:

$$\begin{cases} V_q = R_s I_q + \omega_r (L_d I_d + \lambda_r) + \frac{d}{dt} L_q I_q \\ V_d = R_s I_d - \omega_r L_q I_q + \frac{d}{dt}(L_d I_d + \lambda_r) \end{cases} \tag{20}$$

Therefore, the electromagnetic torque [Nm] in this type of electric motor is expressed as follows:

$$T_e = \frac{3}{2}\frac{P}{2}\left(\psi_r I_q + \left(L_d - L_q\right) I_d I_q\right) \tag{21}$$

where P in Equation (22) is the number of pole and for the PMSM, the d-axis inductance is equal to the q-axis inductance [H]. Therefore, Equation (22) becomes:

$$T_e = \frac{3}{2}\frac{P}{2}\left(\psi_r I_q\right) \tag{22}$$

The PMSM field oriented control (FOC) approach was studied in detailed and adapted from [44]. Table 5 presents the technical specification of the PMSM and Table 6 presents its four quadrant operation.

Table 5. PMSM Technical Specifications [35].

Parameter	Value	Symbol [Unit]
Motor Maximum Power	82.3	P_m [kW]
Motor Maximum Torque	173	T_m [Nm]
Motor Maximum Speed	8000	ω_m [rpm]
Time Constant	0.02	τ [s]
Series Resistance	0	R_s [Ω]
Rotor Inertia	0.00039	I_r [kg $\cdot$ m^2]
Rotor Damping	0.00001	D_r [Nm $\cdot$ s/rad]

Table 6. PMSM Four Quadrant Operation [35].

Quadrant	Operation	Speed	Torque
1	Forward Acceleration	Positive	Positive
2	Forward Braking	Positive	Negative
3	Reverse Acceleration	Negative	Negative
4	Reverse Braking	Negative	Positive

The four quadrant operation of the motor is used when the vehicle is accelerating or decelerating. When the vehicle accelerates, the motor operates in the first quadrant, and its speed and torque are both positive. In this way, the motor converts electrical energy into mechanical rotational motion, supporting the vehicle's movement. When the car decelerates, the motor acts as a generator and converts the mechanical energy into electrical energy, thus opposing the vehicle's motion. The electrical losses of the three-phase model were used to simulate the electric car at the system level, which captures the behavior of the complex model.

Electric Mode Gearbox Design and Gearshift

Table 7 presents the initial parameters of the gearbox and how it was used to obtain the new gear ratio of the e-motor mode such as 1.54, 3.4, and 2.33. A Single-speed gearbox was designed for the simulated hybrid model with respect to the different test profile.

Table 7. Gearbox Parameters [35,45].

Diameter [mm]	Axial Module [mm]	Number of Teeth
d_1	2.25	26
d_2	2.25	40
d_3	2.5	20
d_4	2.5	68
d_5	3	18
d_6	3	42

Figure 10 shows the location of the new gearbox designed located at the real wheel of the vehicle.

Figure 10. New Gearbox Location on the Vehicle adapted from [45].

2.5. Vehicle Monitoring

The CAN data bus facilitates data transmission between control units within the vehicle. It utilizes two data lines to transmit data, enabling efficient communication between various components in the car [46]. This article uses online data collection to monitor the vehicle's electric mode, while the VAG-COM diagnostic system (VCDS) is employed to collect engine data via onboard diagnostics-II (OBD-II). The electric mode results presented in this article are the same as those reported in our previous paper [36] and are reused here for further analysis. However, we can build upon our prior research and conduct additional investigations by leveraging these existing results.

2.5.1. Data Collection Using NetCAN Plus 110

The following hardware already implemented on the car were interconnected used in facilitating the data collection based on HIL method:

- Phoenix Contact Industrial Box PC
- Phoenix Contact Quint Power Supply Unit
- Phoenix Contact WLAN 5100
- Vision Systems GMBH Net CAN Plus 110 (×4)
- Phoenix Contact Wireless Module—FL Timeserver NTP

The sets of the equipment adapted for the HIL experiment were sourced from PHOENIX CONTACT GmbH and Co. KG flachsmarktstraße 8, 32825 Blomberg, Germany. The Lenovo PC is connected to the Phoenix Contact Industrial Box PC remotely via a Local Area Network using an ethernet cable. The LabVIEW software (version: 20.0, 64-bit) runs on this Lenovo PC to read the Can Messages from the Electric Vehicle through the four (4) Net CAN Plus 110 devices. Figure 11 shows the experimental set up for the online CAN bus data measurement. Figure 12 shows the block diagram of the redesigned VW Crafter hybrid vehicle with the data acquisition method installed.

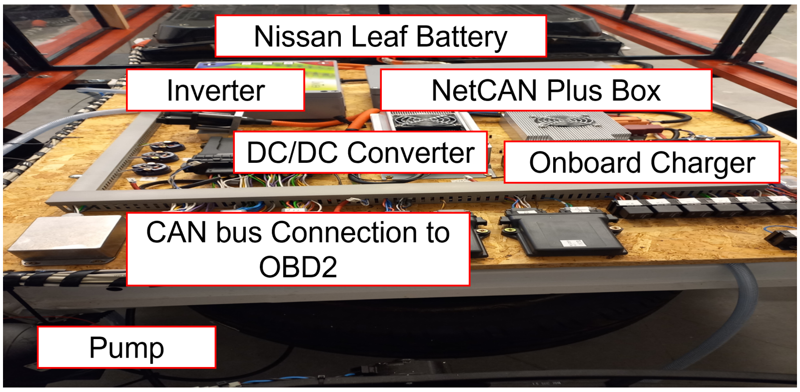

Figure 11. Experimental Setup based on HIL Method [35].

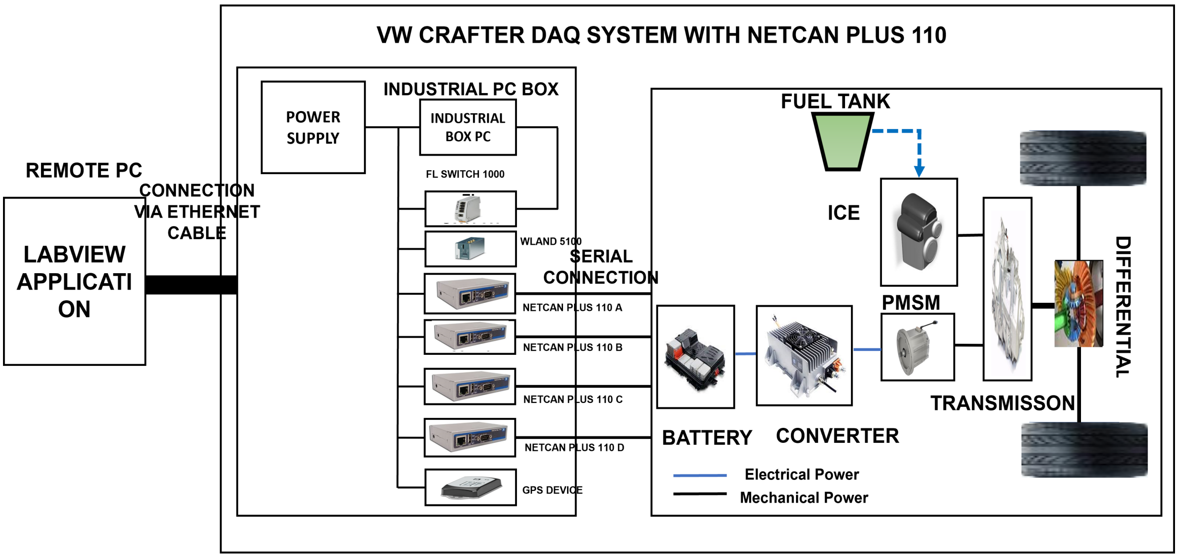

Figure 12. Redesigned VW Crafter Hybrid Architecture modified from [36].

The application is run on the LabVIEW platform; it receives inputs of the IP Address, the Port number of the Net CAN plus 110 devices, and the BUS Speed of 500 Kbps. However, the user clicks on the Open button, and the CAN Channel opens to connect to the Net CAN plus 110 devices to READ the CAN data from the car.

After the design process, the vehicle was then reassembled and formed a hybrid, as shown in Figure 13.

Figure 13. Assembled VW Crafter [45].

2.5.2. Data Collection Using VCDS Scan Tool

The VCDS software (https://www.ross-tech.com/vag-com/VCDS.php, accessed on 10 December 2023) has been used to diagnose and troubleshoot vehicles from the VW group. It is used to collect data from the vehicle's CAN bus for analysis. The data is usually collected by establishing a connection between the OBD-II port and the PC (personal computer) via a VCDS-compatible interface cable.The data collected from the vehicle can be analyzed to diagnose issues or optimize the vehicle's performance. The literature studies revealed that many authors have used VCDS for CAN bus data collection [46–49]. Figure 14 shows the set up for the data collection using the VCDS software.

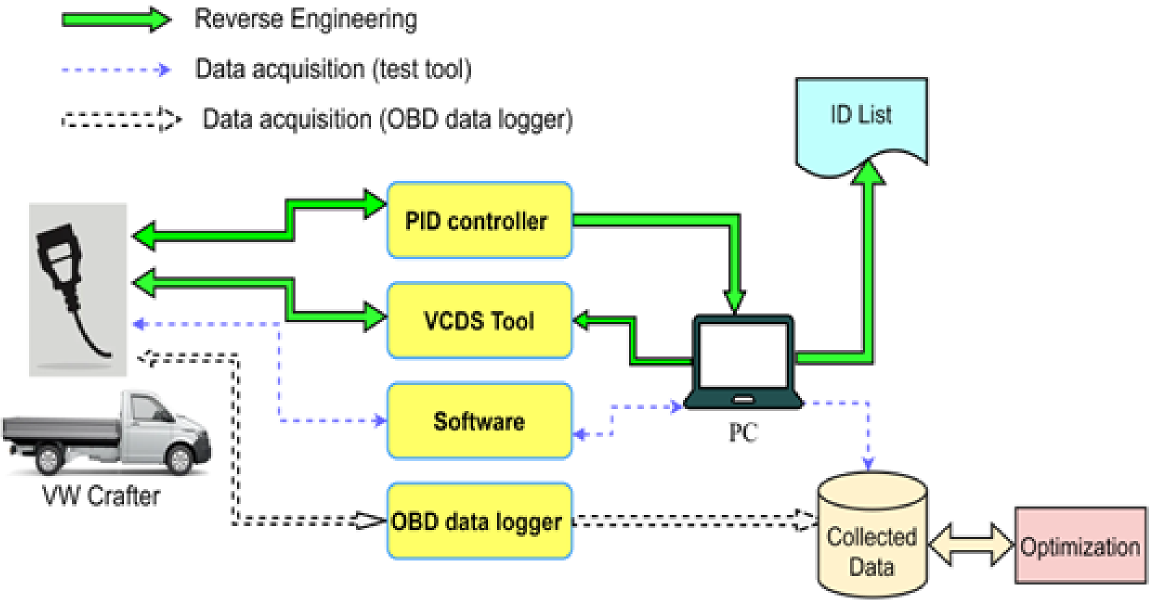

Figure 14. Data Collection Set Up Architecture adapted from [48].

3. Control Strategy Development and Optimization

3.1. PID Controller

PID controller is a simple process controller that consists of three control terms: proportional, integral, and derivative. PID control strategy has been adopted in various industrial applications due to its simplicity, easy troubleshooting, and straightforwardness in implementation [50]. The PID control has been applied for many control applications, such as Quadrotor [51,52], power system [53,54], brushless direct current (BLDC) motor [55,56], and many other applications. Figure 15 shows the detailed block diagram of the PID control strategy for controlling the vehicle speed [km/h], as described in Figure 6 and the reference speed or drive cycle [km/h] is the input to the controller. The PID controller provides the optimal torque [Nm] and speed to the motor [rpm], which regulates the vehicle's speed for optimal consumption. The VW Crafter powertrain represents the vehicle subsystem containing the powertrain, including the engine/motor, battery, and transmission (gearbox), as described in the block diagram of Figure 6. The engine is controlled by its separate PID controller in the engine management responsible for the optimal torque and speed from the engine.

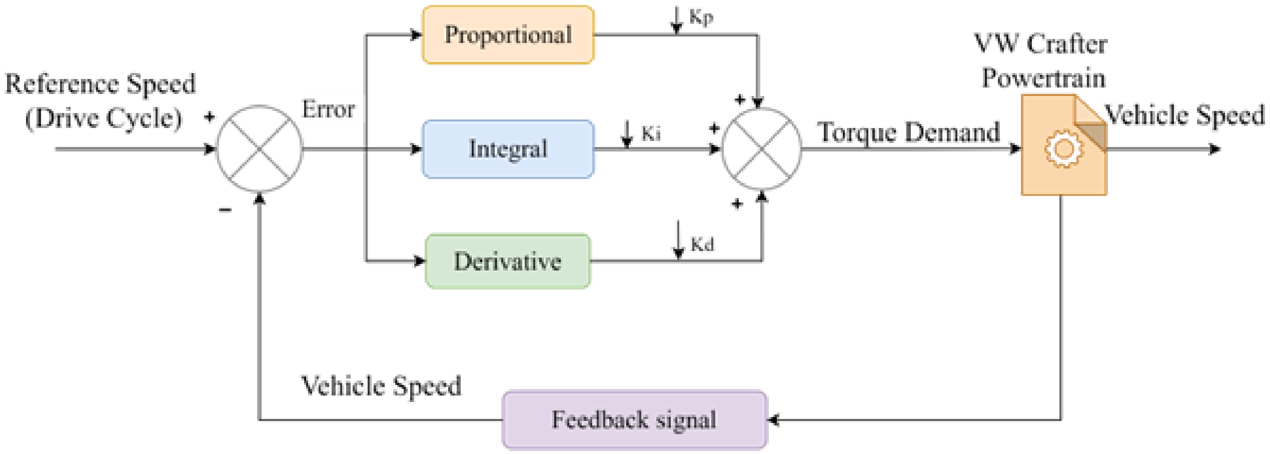

Figure 15. Classical PID Control Architecture.

The PID can be expressed mathematically in s-domain ($G(s)$), which can be expressed as in [57] as follows:

$$G(s) = K_p + \frac{K_i}{s} + K_d s \tag{23}$$

where K_p is the proportional gain, K_i is the integral gain, and K_d is the derivative gain. These parameters determine the performance of the controller. The trial and error method for determining the values of this gains is time consuming and may not yield satisfactory performance for nonlinear system. Therefore, the nonlinear dynamics of the HEVs system, disturbances, and other external effects, necessitate the optimal design of the PID controller in this research. As a result, an enhanced GA-PID is proposed in order to achieve an optimal balance between the K_p, K_i, and K_d for the desired performance.

3.2. Meta-Heuristic Optimization of the PID Controller

3.2.1. GA-PID Controller

The traditional tunning approach, such as trial and error and Ziegler-Nichols methods combined in a heuristic, makes achieving optimal performance difficult, especially for nonlinear dynamics systems [58]. Therefore, more advanced design approaches for the PID control have been adopted to handle the issue of nonlinear effects, such as fractional-order PID (FOPID) in [59], PSO-PID in [60], fuzzy PID in [61,62]. However, the GA is an optimization algorithm inspired by the principles of natural selection. The GA is applied to find the optimal solution to complex problems. For example, it is utilized to find optimal solutions in control systems in machine learning (ML), scheduling, tuning controllers such as PID, NN, fuzzy logic, and so on. Figure 16 shows the steps or process in flowchart for tuning the PID controller using GA. While Figure 17 shows the enhanced PID structure based on the GA technique used to obtain the optimal gains of the classical PID controller of Figure 15 to reduce the fuel consumption and CO_2 emission for designed hybrid Crafter in this research.

The following are the detailed steps for PID tuning using GA as illustrated in Figure 16 and implemented on Figure 17: Step 1. The initial random population should be generated. Therefore, in this case, every individual represents the three control gains of the PID controller such as K_{pi}, K_{ii}, K_{di}, where i = 1, 2, . . ., . . . ps and ps is the ith individual gain from the total number of individuals from the population. Step 2. Initialize the PID parameters' lower and upper bound values, such as the Kp, Ki, and Kd values. Step 3. Encode the PID parameters, i.e., K_p, K_i, and K_d parameters, into strings known as chromosomes. Step 4. Define the error criteria, such as the value of fit (fitness value) such as ITAE. The error criteria are defined in terms of the PID integral square error, such as the integral. These values of error should be minimum if maximum iteration is met. The following equations define the mathematical formulations of the errors as expressed in [63]:

$$\begin{cases} IAE = \int_0^\infty |e(t)|dt \\ ISE = \int_0^\infty |e(t)|^2 dt \\ ITAE = \int_0^\infty t|e(t)|dt \\ ITSE = \int_0^\infty t|e(t)|^2 dt \end{cases} \tag{24}$$

where IAE is the absolute error, ISE is the integral square error, ITAE is the integral time absolute error, and ITSE is the integral time square error. Step 5. Apply the operators of the GA techniques, i.e., reproduction, mutation, and crossover, to evaluate the fitness value for every chromosome (the encoded Kp, Ki, Kd of the PID controller). Step 6. Decoding. Step 7. This is called the evaluation criteria. In this step, check if the fitness value (error) is minimum. If yes, go to step 8; if not, go back to step 4. Step 8. The best values of the PID parameters are found.

Therefore, in this research, the algorithm is repeatedly used to refine a population parameter setting using selection, crossover, and mutation operations until it converges on a solution that represents minimum values of the objective functions (in this case, the errors), which gives optimum tuning for the PID parameters. However, the set-point refers to the desired vehicle speed, which serves as the reference input for the PID controller. The controller's input signal is the speed error, e(t), calculated as the difference between the reference speed (drive cycle in km/h) and the vehicle's actual speed (also in km/h). This error signal enables the PID controller to generate the appropriate control signal to regulate the vehicle's speed. In addition, the controller determines the required motor and engine speed and torque for propelling the vehicle's wheels. The entire system model, comprising the battery, electric motor, and vehicle systems, is integrated into an optimization framework based on the proposed optimization method to minimise fuel and energy consumption and reduce CO_2 emissions. This framework optimizes the vehicle's energy consumption by iteratively searching for the optimal control parameters. Table 8 presents the parameters used to tune our PID parameters based on the GA technique.

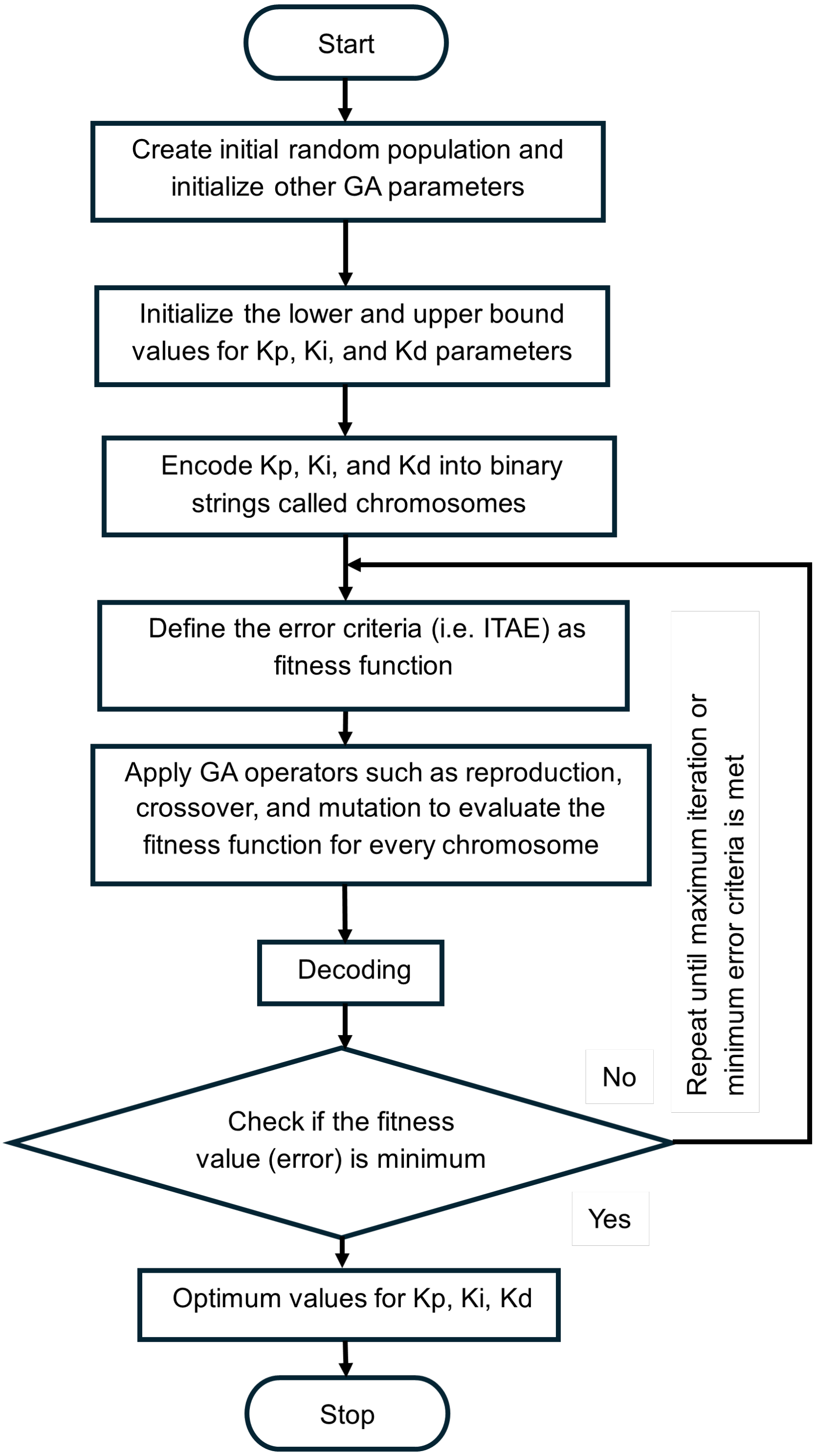

Figure 16. GA-PID Flowchart [63].

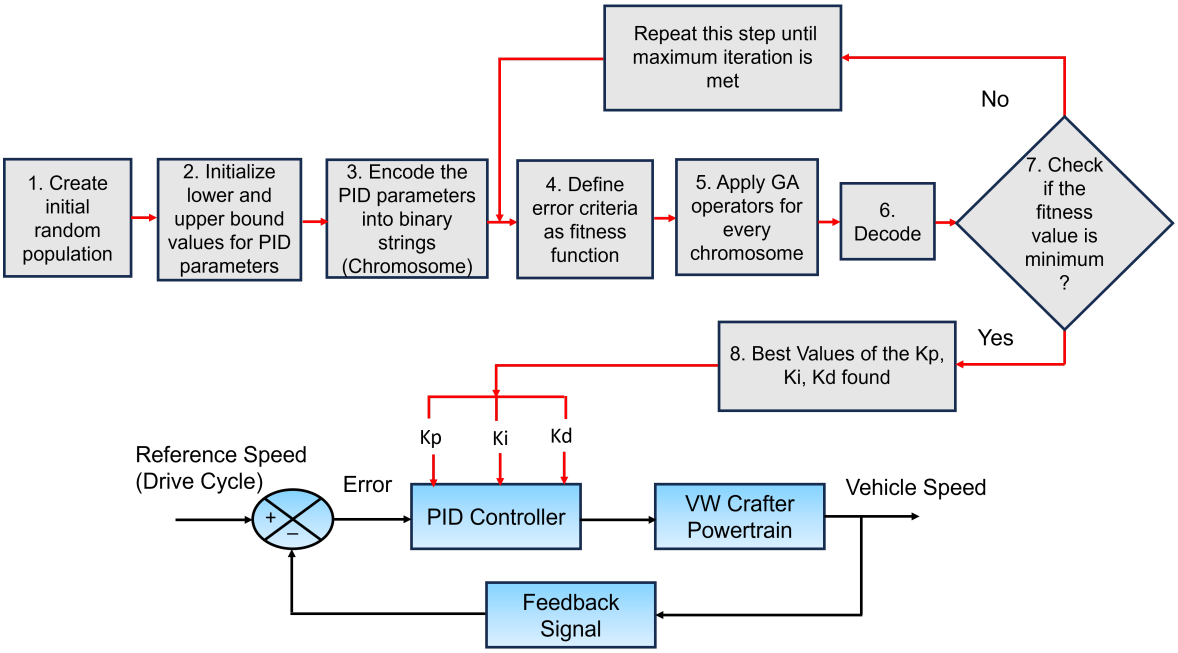

Figure 17. GA-PID Control Structure adapted from [63,64].

Table 8. Genetic Algorithm Parameters.

Parameter	Value
Selection Strategy	Random
Fitness Performance	Proportional
Generations	40
Population Size	100
Number of Variables	3
Lower Bound [LB]	[0 0 0]
Upper Bound [UB]	[2000 2000 2000]

3.2.2. PSO-PI Controller

PSO is a meta-heuristic technique inspired by the behavior of social animals such as birds. It is based on the population attributed to Kennedy and Eberhart in 1995 [65], which was meant to simulate social behavior. The PSO is inspired by the foraging strategy seen in bird flocks in which individuals are guided by their knowledge, momentum and collective wisdom to move towards the most favorable food sources [29]. The PSO technique emulates this behavior by representing each solution as a particle with global and personal positions and inertia [29]. Therefore, each particle has certain features, i.e., velocity, position, and objective, which strive to attain convergence toward global optimum through a series of iterations [29]. In PSO algorithm, each particle searches constantly for the best position in the multidimensional space. Therefore, the flying particle in PSO algorithm is changing its position on the basis of its experience with the position of the neighboring particles, keeping its previous position and its neighboring particles. During this process, the individual particles have undergone a change in position influenced by the flying particles' experiences and that of their neighbors [65]. Therefore, the velocity and position for the particles are updated as expressed in [65] as follows:

$$\begin{cases} V_i^{k+1} = w \cdot V_i^k + C_1 \cdot \mathrm{rad}_1 \cdot \left(P^{\mathrm{lbest}} - P_i^k\right) + C_2 \cdot \mathrm{rad}_2 \cdot \left(P^{\mathrm{gbest}} - P_i^k\right) \\ P_i^{k+1} = P_i^k + V_i^{k+1} \end{cases} \tag{25}$$

where P_i^k, V_i^k, C_1, C_2, w, P^{lbest}, P^{gbest} are particle's position, velocity, acceleration coefficients, inertia weight, local best position, global best position, and $rand_1$ and $rand_2$ are the random number between 0 and 1 [65]. However, the parameters of the PID (PI in this case) controller were tuned using the PSO algorithm since it can be find the optimal solutions to a nonlinear and complicated system [65]. Therefore, Table 9 presents the simplified parameters of the PSO used based on the ITAE objective function to get the optimal control parameters. Figure 18 shows the flowcart of the PSO-PI strategies.

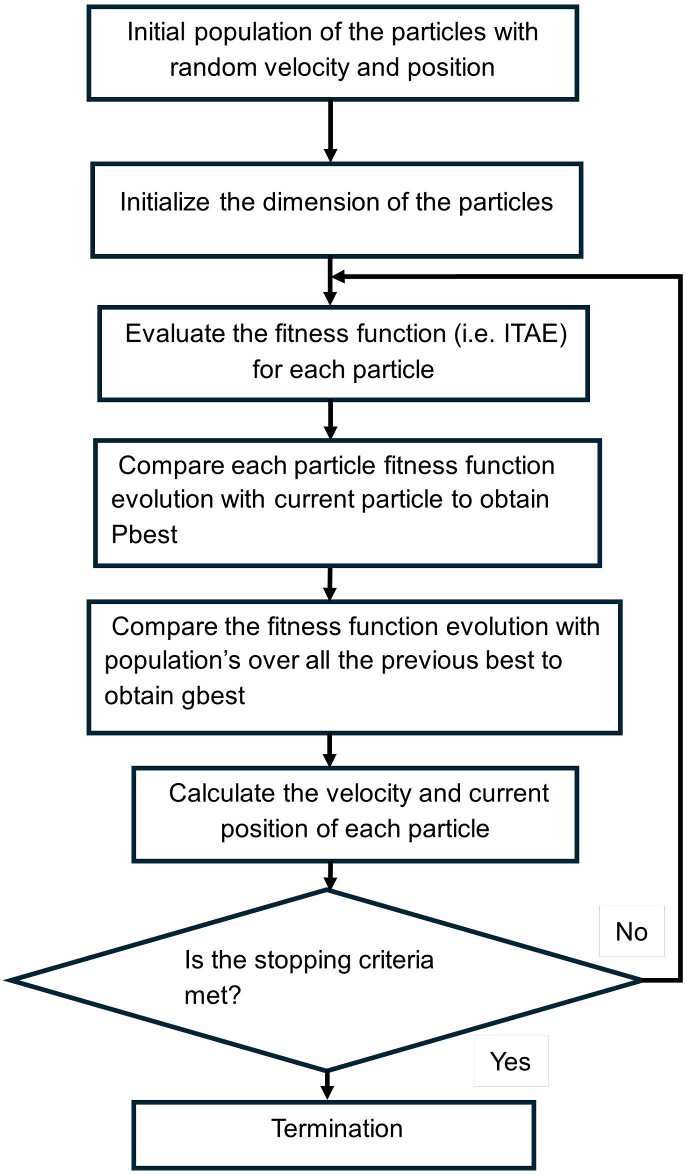

Figure 18. PSO-PI Flowchart [66].

Table 9. PSO Parameters.

Parameter	Value
Number of Particles	100
Number of Iterations	300
Number of Variables	2
Lower Bound [LB]	0
Upper Bound [UB]	6000
Cognitive Coefficient (c)	1.9
Inertia Weight (w)	0.09

3.3. Fractional Order PID Controller

In recent years, the application and popularity of fractional calculus have been increasing in the scientific and engineering fields since its introduction about 3000 years ago. It generalizes the classical integer order differential and integral calculus to the non-integer order. Based on this concept, the famous classical PID has been enhanced and expanded to include two more parameters and became FOPID. Therefore, to design the FOPID, Figure 15 of the classical PID should be modified by adding one block in cascade to each of the integral and derivative blocks and the transfer function is modified as expressed in [67] as follows:

$$G(s) = K_p + \frac{K_i}{s^{\lambda}} + K_d s^{\mu} \tag{26}$$

where $\frac{1}{s^{\lambda}}$ and s^{μ} are fractional integral and fractional differential operators [67].

4. Model Development and Simulation

4.1. The Conventional VW Crafter Development

The conventional VW Crafter based on the model-in-the-loop (MIL) approach was simulated in MATLAB software (R2024a version). The model comprises various subsystems such as the drive cycle, the vehicle controller, the engine, the torque/speed sensor, the transmission, the gearbox controller, the tire and vehicle dynamics subsystems. The proposed engine in this research made in 2012 and complied with the euro 6d emission standard, is based on the 2.0 TDI CR diesel engine, which has replaced a 2.5 TDI CR diesel engine. The study in [45] reaffirmed that the 2.5 TDI CR diesel engine had a turbo failure problem, necessitating its redesign in 2010 and an updated version that used diesel exhaust fluid (DEF) combined with DPF, which complies with the euro V emission standard. The 2.0 TDI was chosen due to its higher output torque, reduced consumption, and lower emission compared to the 2.5 L TDI engine. The proposed engine features a displacement of 1968 cc, an approximately 8–900 km range, and a tank capacity of 70 L. The conventional VW Crafter vehicle's powertrain consists of a mechanical drivetrain comprising a transmission and driveline. The transmission includes a disc friction clutch and a six-speed manual gearbox, while the driveline consists of the driveshaft and final drive. Real-world driving scenarios based on WLTP were simulated to assess the vehicle's fuel consumption, serving as a benchmark for the hybrid powertrain design. Figure 19 shows the MATLAB (R2024a) model of the conventional VW Crafter with modeling approach adapted from [68].

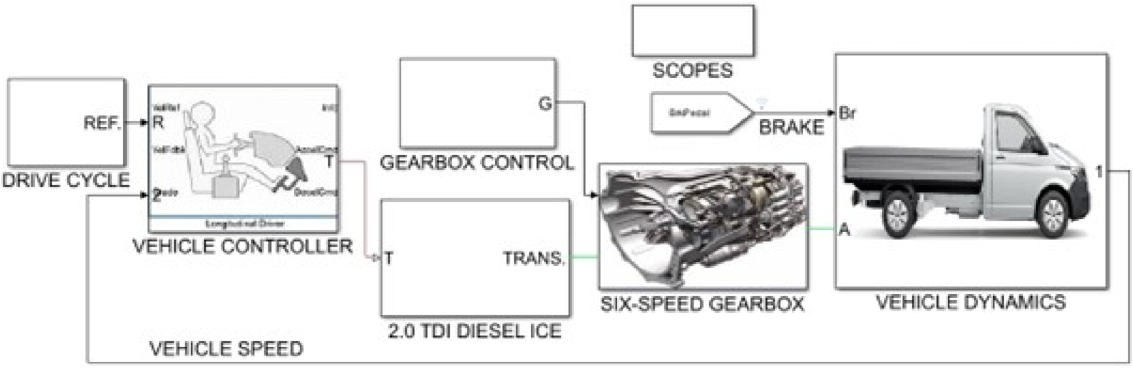

Figure 19. The Conventional Vehicle Model.

4.2. The Hybrid VW Crafter Development

The aim of the hybrid technology is enhancing the system's efficiency [69]. In this article, the permanent magnet synchronous machine was incorporated with the 2011 Nissan Leaf battery pack to facilitate the hybrid powertrain design from the conventional Crafter. This design aims to reduce fuel consumption and CO_2 emissions and optimize the overall performance. A PID controller was designed based on the meta-heuristic techniques to control vehicle speed and provide optimal torque for minimal fuel consumption. Figure 20 shows the MATLAB (R2024a) model for the transformed VW Crafter hybrid powertrain.

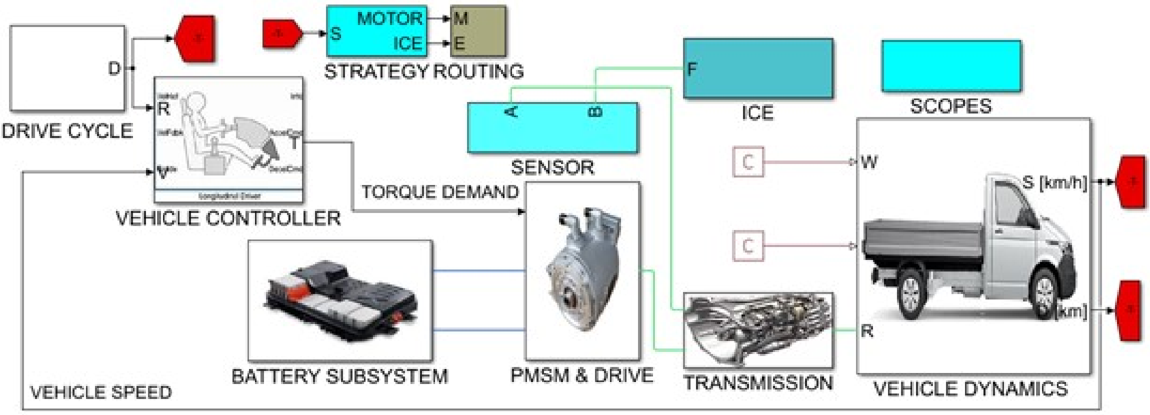

Figure 20. The hybrid Vehicle Model.

5. Results

This research uses MATLAB's Simulink and Simscape toolboxes to design the vehicle. Therefore, developing the optimization algorithm for the physical model is tricky. This research uses a system identification technique to estimate the mathematical model of the system in the frequency domain for the more straightforward implementation of the optimization algorithms. In this section, the simulation and experimental results for the VW Crafter's conventional and hybrid powertrains are presented. Table 10 presents the gains of the classical PID and the GA-PID and PSO-PI found based on the ITAE objective function. For GA-PID, K_p, K_i, and K_d were 70.6657, 0.3339, and 72.4406, respectively. For PSO-PI, K_p and K_i, were 1243.1 and 1.3453, respectively. While Table 11 presents the gains of the FOPID controller.

Table 10. Classical PID, GA-PID, and PSO-PI Gains.

Gain	Classical PID	GA-PID	PSO-PI
K_p	60	70.6657	1243.1
K_i	10	0.3339	1.3453
K_d	60	72.4406	-

Table 11. Fractional order PID Gains.

Gains	Value
K_p	1000
K_i	20
K_d	0.05
$lamda\ [\lambda]$	0.5
$mu\ [\mu]$	0.02

Figure 21 shows the achieved vehicle's speed due to the WLTP drive cycle. The vehicle speed has tracked the reference speed with a minimal deviation at some point due to the system complexity and approximation during the system's identification process. The performance of the proposed control strategy was found to be more effective than the PSO-PID and FOPID strategies in terms of the energy consumption and system's energy and power efficiency. However, it was found that the derivative part did not perform well in the system response due to noisy signals, which would take more time to converge to the optimal solutions. Therefore, a PSO-PI and FOPID control strategies were used to compare and verify the effectiveness of our proposed control algorithm (GA-PID).

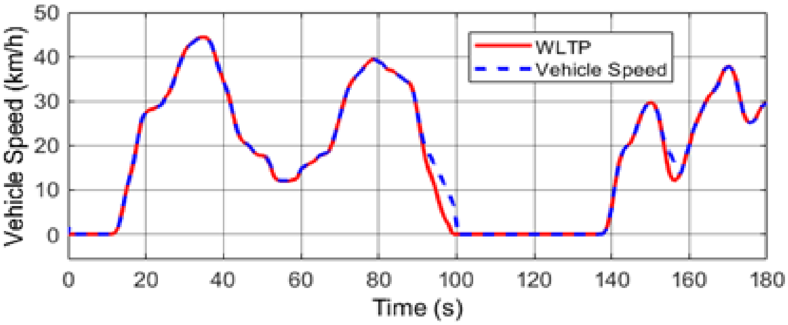

Figure 21. VW Crafter Speed due to WLTP test Procedure.The vehicle speed has successfully tracked the reference speed with a minimal deviation at some point. This is attributed to the system's complexity and nonlinear nature.

Figures 22 and 23 show the power and energy consumed by the Nissan Leaf battery and the electric motor. However, the positive portion of the energy in Figure 20 represents the energy consumed, while the negative part due to the drive cycle represents the energy recovery. The energy consumption and recovery concept for an electrical machine was investigated by Parczewski, K. in [70]. For the GA-PID control strategy (with optimal control gains of 70.6657, 0.3339, and 72.4406), the energy consumed by the battery and motor was 0.1295 kWh/km (12.95 kWh/100 km) and 0.1162 kWh/km (11.62 kWh/100 km). The power consumed by the battery and motor was 50.80 kW and 44.94 kW. The energy and power efficiencies are approximately equal, which were 89.73% and 88.46%, respectively.

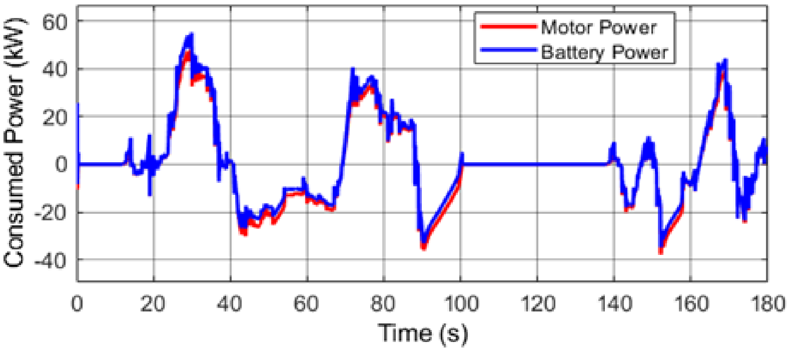

Figure 22. Electrical and Mechanical Power due to WLTP test Procedure. The red line represents the motor consumed power which stands at 50.80 kW peak. While the blue line represents the battery power which stands at 44.94 kW.

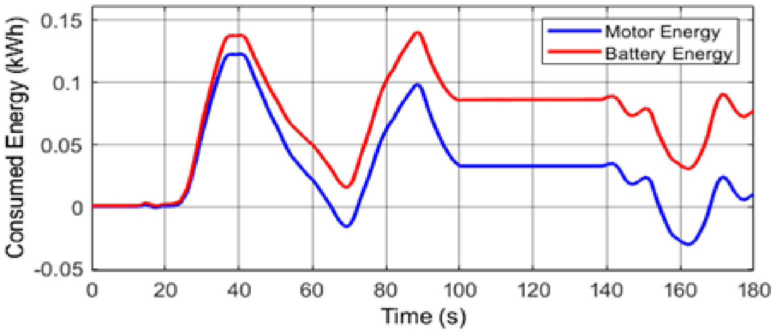

Figure 23. Electrical and Mechanical Energy due to WLTP test Procedure. The electrical energy represents the battery consumed energy which is the red line in this case, and the blue line which represents the energy consumed by the PMSM.

Moreover, For the PSO-PI control strategy (with optimal control gains of 1243.1 and 1.3453), the energy consumed by the battery and motor was 0.1403 kWh/km (14.03 kWh/100 km) and 0.1228 kWh/km (12.28 kWh/100 km). The power consumed by the battery and motor was 55.06 kW and 48.61 kW. The energy and power efficiencies are approximately equal, which were 87.53% and 88.29%, respectively. At the same time, the consumed battery and motor power for the FOPID strategy were 54.99 kW and 48.56 kW and energy consumption were 14 kWh/100 km and 12.28 kWh/100 km, respectively.

Figures 24 and 25 show the simulated battery current capacity and the SOC due to the drive cycle test procedure. The maximum current capacity was 66.2 Ah, the minimum capacity consumed was 65.85 Ah, and the final steady capacity was 66.02 Ah, as shown in Figure 24. Similarly, The SOC of the battery was approximately 99.8%, as shown in Figure 25.

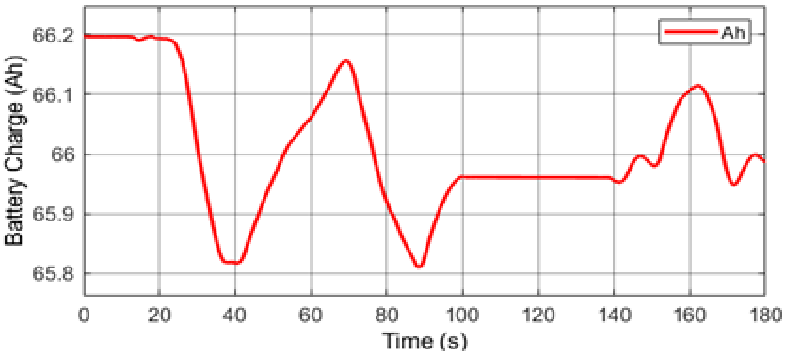

Figure 24. Battery Charge due to WLTP test Procedure. The maximum current capacity of the 2011 Nissan Leaf pack is 66.2 Ah. Each of the battery has a capacity of 33.1 Ah at the 0.3 C rating for the design specification. For EV application, the C rating stands at 2 C–5 C to give enough current for the system.

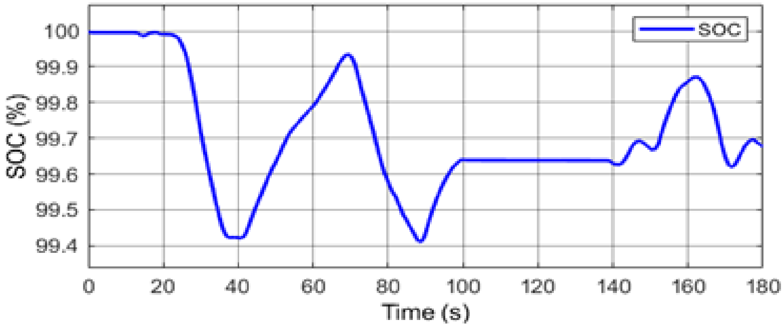

Figure 25. Battery SOC due to WLTP test Procedure. This is the battery state of charge at the current capacity represented in figure. The initial state of the charge was at 100% and the simulations ran up to 180 s.

Figures 26–30 show also the simulation results for the VW Crafter model. Figure 26 shows the HEV engine speed (3662 rpm), Figure 27 shows the fuel flow for the hybrid Crafter (approximately 2 g/s), Figure 28 shows the conventional Crafter engine torque (67.12 Nm and −67.12 Nm), Figure 29 shows the conventional Crafter fuel flow (3.781 g/s), and Figure 30 shows the engine and motor power (31.6 kW and 44.94 kW), respectively, for the hybrid vehicle due to the WLTP drive cycle test. The fuel flow of 2 g/s is translated to an equivalent cumulative fuel consumption of 3.069 L/100 km due to the drive cycle test at the controller gains of [70.6657, 0.3339, 72.4406]. Therefore, the value of the fuel consumption of 3.069 L/100 km from the fuel consumption resulted from the cumulative sum of the fuel flow in g/s due to the drive cycle at a speed of 44.5 km/h.

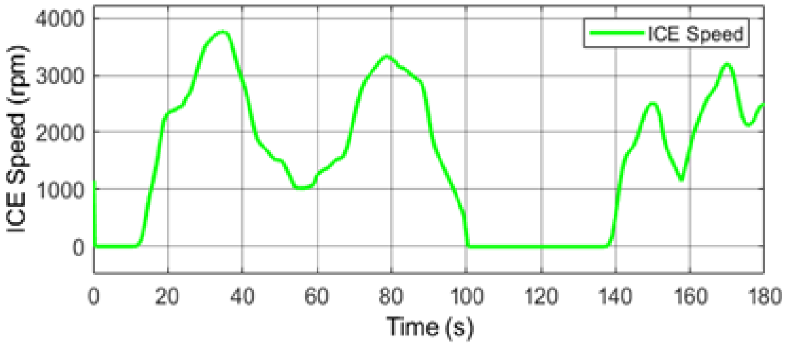

Figure 26. ICE Speed due to WLTP test Procedure.TThe simulated ICE maximum speed stands at 3662 rpm at 180 s for the simulations and the speed was steady at 2500 rpm.

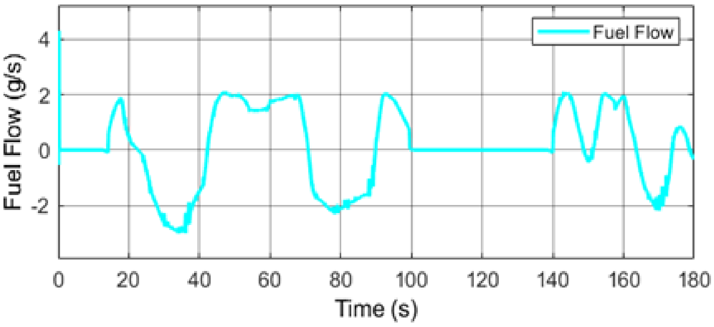

Figure 27. Hybrid VW Crafter Fuel Flow due to WLTP test Procedure. The maximum fuel flow of 2 g/s which stands at 3.069 L/100 km.

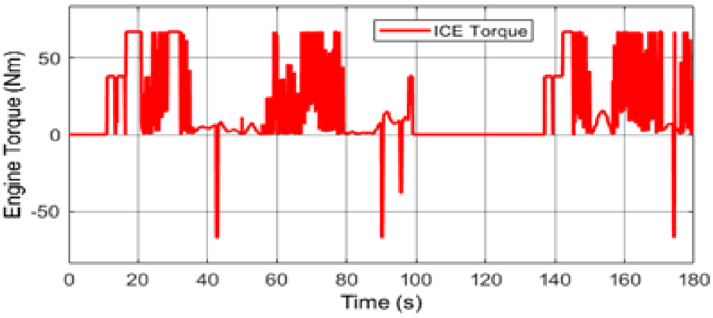

Figure 28. Conventional VW Crafter Torque to WLTP test Procedure. This represents the simulated torque for the vehicle at 180 s.

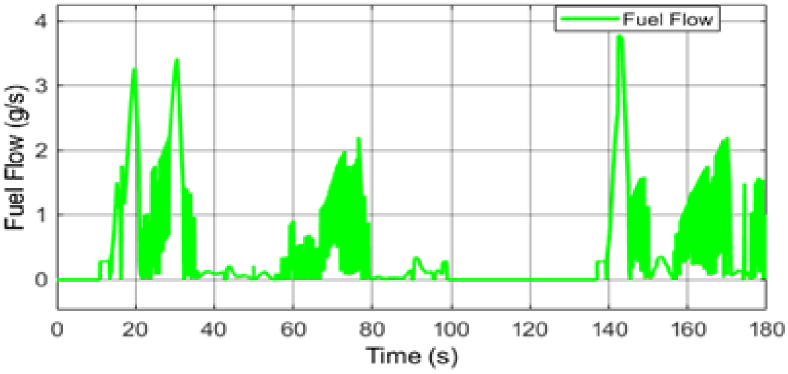

Figure 29. Conventional VW Crafter Fuel Flow due to WLTP test Procedure. The fuel flow or fuel consumption of the conventional VW Crafter stands at 3.781 g/s which cumulatively stands at 9.739 L/100 km.

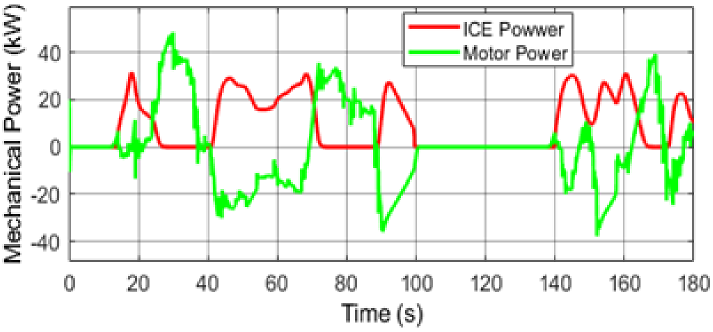

Figure 30. Motor and ICE Power due to WLTP test Procedure. The motor and engine power gave the total mechanical power that is translated to the vehicle's movement.

However, the engine torque achieved was 67.12 Nm and −67.12 Nm. This torque is considered the operating torque as at the simulation time of 180 s. We have analyzed the wheel torque (7727.186 Nm) that would be required by this vehicle for the WLTP drive which has a maximum speed of 131 km/h Therefore, a high torque is essential for tackling uphill climbs and hauling heavy loads for the VW Crafter light commercial vehicle. Enhanced continuous operating torque directly correlates with exceptional acceleration capabilities. Increasing torque can significantly enhance dynamic performance if rapid acceleration is a top priority. Moreover, higher torque can optimize energy recovery during regenerative braking, improving overall energy efficiency, particularly in typical urban driving scenarios with frequent stops and starts. However, torque requirements may vary depending on driving conditions, with higher torque benefiting city driving and lower torque suiting highway cruising.

Figures 31–33 compare the simulated and experimental results obtained using the CAN bus measurement method. These experimental results have been adapted from our previous publication and are being reused in this article for further analysis [36]. The experimental verification of the theoretical findings was carried out to understand vehicle performance and behaviours. One of the means of obtaining information about the modes and operation of cars is from the CAN messages, also known as CAN frames. In order to collect the vehicle's CAN Bus data, four Net CAN plus 110 devices were utilized facilitated by the network connection to the vehicle system, each with a unique IP address: a. 192.168.10.13: Charging data, b. 192.168.10.12: Inverter data, c. 192.168.10.10: Temperature data, and d. 192.168.10.11: Auxiliary data. The vehicle was in charging mode during data collection. The LabVIEW application was configured with the IP addresses, port numbers, and a bus speed of 500 Kbps. When the user clicks the 'Open' button, the CAN channel connects to the Net CAN plus 110 devices, enabling the reading of CAN data. Therefore, Figure 31 shows the experimental and simulated vehicle's speed. During the vehicle test on electric mode, the speed was set to 13 km/h, and it was controlled with the help of the PID controller using the same speed as the reference.

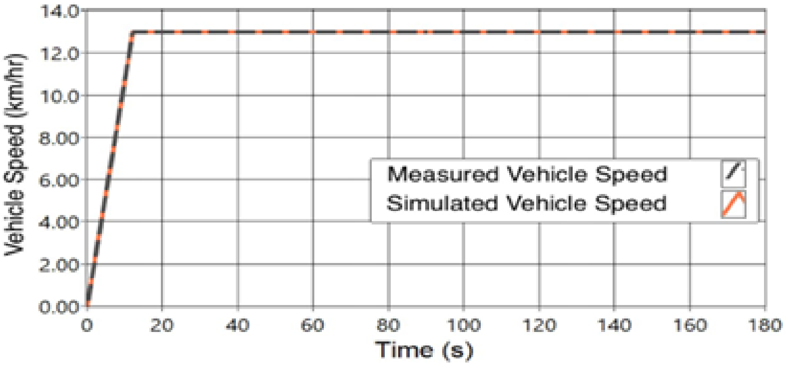

Figure 31. Experimental and Measured Speed.

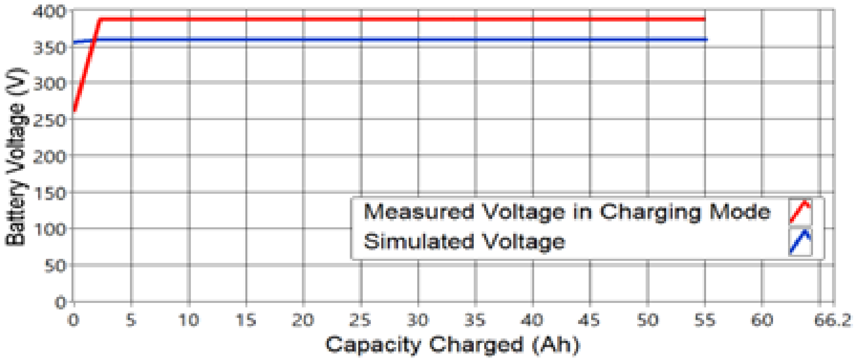

Figure 32. Experimental and Measured Voltage.

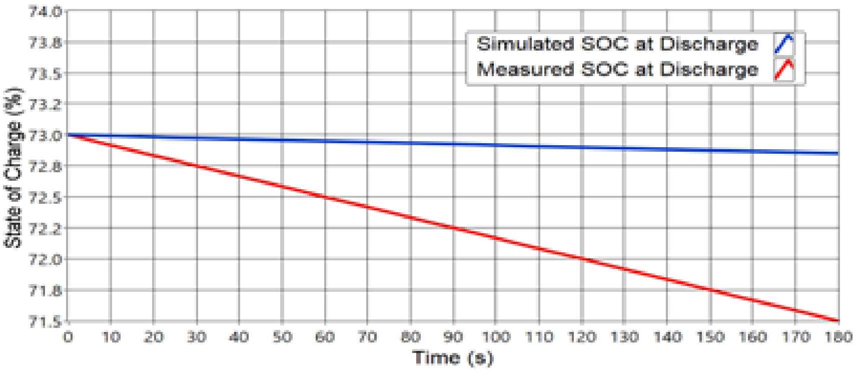

Figure 33. Experimental and Measured Battery Capacity.

Figure 32 shows that the experimental voltage was 388 V, and the simulated voltage was 362.6 V and the nominal voltage is 360 V and steady within 180 s. Figure 33 shows the experimental and simulated current capacity during discharging. The initial capacity was 55 Ah, the measured capacity decreased to 53.5 Ah, and the simulated capacity decreased to 54.7 Ah.

Figures 34–36 show the experimental data collected using the VCDS via the vehicle OBD-II. This measurement aimed to compare the vehicle's simulated and experimental fuel consumption. Figure 34 shows the measured engine speed [rpm], vehicle speed [km/h], and the mass airflow (MAF) in milligrams per stroke [mg/str] for the conventional vehicle. The maximum MAF was 1138 mg/str at an equivalent 2743 rpm engine speed, translating to a large fuel flow during this period. Therefore, we adapted mathematical formulations to get a reliable fuel flow and considered the flow over the whole journey during the test. The MAF at 180 s was measured to be 490 mg/str at the engine rpm of 2310 rpm. The vehicle speed at this MAF and engine rpm were measured to be 108 km/h. The MAF [g/s] was calculated to be 56.5905 g/s. Since our diesel engine's air-fuel ratio (AFR) is 14.5, then the equivalent mass fuel flow (MFF) would be 3.9 g/s. Therefore, the equivalent volume flow rate was 17.1342 L/h (15.5766 L/100 km at a vehicle speed of 108 km/h) using the density of the diesel fuel, 820 g/L. Therefore, the estimated experimental fuel consumption for the VW at 44.5 km/h was 6.4181 L/100 km. Figure 35 shows the specified boost pressure of 10,275 millibar [mbar] and the actual boost pressure of 11,645 mbar at 180 s. Figure 36 shows the MAF of 385 mg/str and engine speed of 450 rpm at 180 s measured in an idle situation.

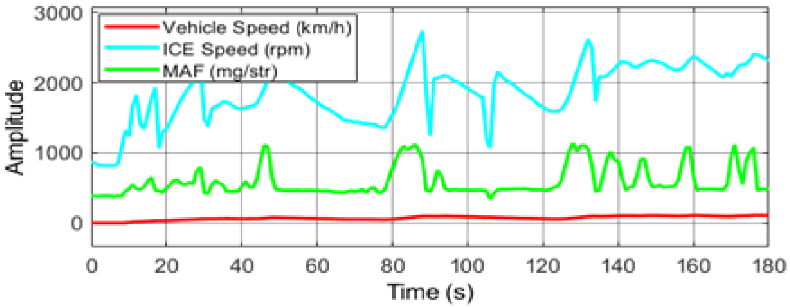

Figure 34. Experimental Mass Air Flow rate, Vehicle Speed, and Engine Speed.

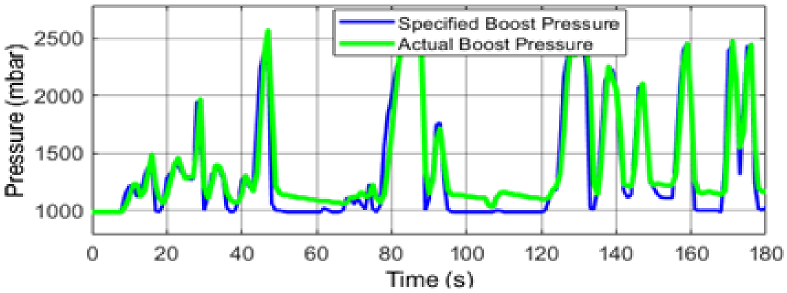

Figure 35. Specified Boost Pressure and Actual Boost Pressure.

Table 12 presents the fuel and energy consumptions and CO_2 emissions based on the different control strategies. The GA-PID achieved 3.069 L/100 km with 74.79 gCO_2/km, the PSO-PI achieved 2.203 L/100 km with 53.58 gCO_2/km, and FOPID achieved 2.229 L/100 km with 54.1743 gCO_2/km, respectively. At the same time, the energy consumptions were 12.95, 14.03, and 14 kWh/100 km, respectively. Table 13 compares the fuel consumption and CO_2 emissions between the conventional and hybrid VW Crafter models. The traditional VW Crafter achieved fuel consumption of 9.739 L/100 km with 255.4122 gCO_2/km emissions, and the hybrid powertrain achieved 3.069 L/100 km with 74.79 gCO_2/km emissions. This is translated to a 68.49% reduction in fuel consumption when transforming the vehicle from the conventional to hybrid for GA-PID.

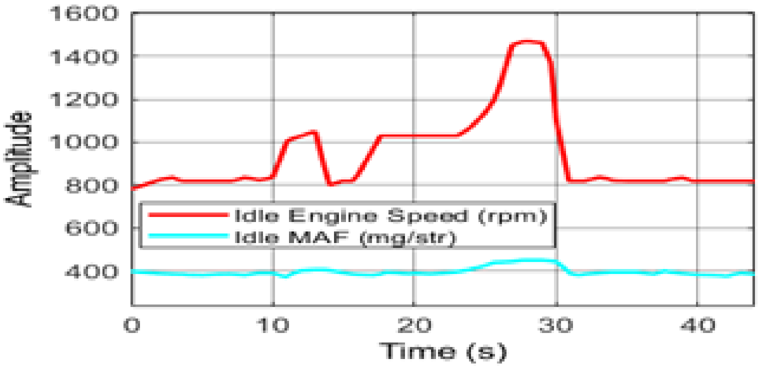

Figure 36. Idle Engine Speed and MAF.

Table 12. Comparison of the Control Strategies.

Control Strategy	L/100 km	MPG	km/L	TFU [L]	[kWh/100 km]	Extension [km]	Emissions [g/km]
GA-PID	3.069	32.59	76.65	0.02801	12.95	185.32	74.79
PSO-PI	2.203	45.39	106.8	0.02007	14.03	171.062	53.58
FOPID	2.229	44.86	105.5	0.02029	14	171.43	54.1743

Table 13. VW Hybrid and Conventional Powertrain Fuel Consumption and CO_2 Emissions.

Powertrain	L/100 km	km/L	MPG	TFU [L]	Emissions [g/km]
Conventional	9.739	10.27	24.15	0.09566	255.4122
Hybrid	3.069	32.59	76.65	0.02801	74.79

6. Discussion

This article has presented the studies of the transformation and physical assembly process of the VW Crafter of the faculty of engineering at the University of Debrecen from the traditional ICE-powered vehicle to hybrid, presenting a novel and innovative approach using Netcan Plus hardware devices for the experimental analysis of the vehicle CAN bus system based on HIL method. This approach was used as the basis for the transformation of the VW Crafter conventional powertrain to a hybrid one to optimize fuel consumption and reduce harmful gas emissions, demonstrating significant potential for advancing the understanding and application of hybrid vehicle technologies. The vehicle assembly process involved constructing the hybrid vehicle by incorporating the permanent magnet synchronous electrical machine based on a new designed gearbox in the rear suspension's front, which was coupled to the rear differential through a clutch. The mechanical engineering research group at the University of Debrecen in ref. [45] detailed this assembly process. In [45], the e-drive ignition must be switched ON to activate the electric mode and keep the gearshift in the neural position. Therefore, the vehicle's motion is activated by switching the joystick back and forth for the reverse and forward motion. The vehicle monitoring system, via Netcan plus a hardware framework, aims to conduct the electric drive test. This research has additionally proposed a popular diagnostic tool (VCDS) to test the engine drive and perform a complete study and analysis of the reference vehicle.

The OBD-II dataset for ICE real measurement was adapted from the car manufactured by the VW group with almost the same engine configuration, such as the engine displacement, number of cylinders, fuel system, fuel type and so on, to access the full measurement data. However, the actual fuel consumption may vary due to the unique characteristics of each vehicle. The fuel published on automobiles onboard computers may not be precise. Therefore, to get accurate and reliable fuel consumption, we needed the mass air-fuel flow and the engine speed and adapted the following equations as used in [71,72] to complete the fuel consumption computation:

$$\begin{cases} \text{Fuel Consumption [L/100 km]} = \frac{\text{Fuel Flow [L/h]}}{\text{Vehicle Speed [km/h]}} \cdot 100 \\ \text{Instant. Fuel Consumption [L/km]} = \frac{\text{Fuel Flow [L]}}{\text{Vehicle Distance [km]}} \\ \text{Fuel Fow [L/h]} = \frac{\text{MAF} \cdot 3600}{\text{AFR} \cdot \text{FD}} \end{cases} \tag{27}$$

where MAF is the air mass flow [g/s], AFR is the actual air fuel ratio [14.5 in our case], FD is the fuel density [g/L]. The final fuel consumption can be calculated if either MAF [g/s] or MFF [g/s] is available. This method of estimating the fuel economy based on the measured data is the most accurate and reliable method [71,72]. Therefore, the MAF was calculated to be 56.5905 g/s, and the equivalent MFF was 3.9 g/s. Therefore, the equivalent volume flow rate was 17.1342 L/h (15.5766 L/100 km at a vehicle speed of 108 km/h). Therefore, the estimated experimental fuel consumption for the VW at 44.5 km/h was 6.4181 L/100 km. The measured fuel consumption of 6.4181 L/100 km was as expected, considering the operating conditions and the vehicle speed during the measurement. This shows that there was good fuel economy for the VW Crafter. Our previous paper [36], reported that the measured fuel consumption, according to the manufacturer datasheet, was estimated to be 10.1 L/100 km, and the one manufactured in 2018 was 10.81 L/100 km. However, the VW Crafter manufactured in 2020 showed a fuel consumption of 8.8–10 L/100 km for low (WLTP) speed. However, for the simulation, Figure 29 shows the value of the mass fuel flow of 3.781 g/s for the conventional vehicle, which translated to the cumulative consumption of 9.739 L/100 km. Therefore, considering the manufacturer datasheet, we have achieved good fuel economy even in the case of the simulated conventional Crafter. Similarly, the simulated hybrid vehicle has achieved a mass fuel flow of 2 g/s, which is translated to an equivalent cumulative fuel consumption of 3.069 L/100 km due to the drive cycle test at the controller gains of [70.6657, 0.3339, 72.4406]. This interpretation can be further studied in [73]. Therefore, Table 12 presents different values of the fuel economy achieved and the emissions according to the different PID optimizer and the FOPID. Therefore, the value of the fuel consumption of 3.069 L/100 km from the fuel consumption resulted from the cumulative sum of the fuel flow in g/s due to the drive cycle at a speed of 44.5 km/h. At the same, Table 13 presents the comparison of the fuel economy between the conventional and hybrid model of the VW Crafter.

The successful transformation of the VW Crafter from conventional to hybrid has been achieved, resulting in optimized fuel and energy consumption through an enhanced PID controller. The controller was used as EMS, controlling the vehicle speed and allocating the optimal speed and torque to the powertrain for the optimal consumption. The GA-PID achieved an optimal fuel consumption of 3.069 L/100 km for the hybrid powertrain. The conventional powertrain achieved 9.739 L/100 km with a classical PID but tuned with the help of a trial and error method. This shows a 68.49% reduction in the fuel consumption. In the case of PSO-PI, the fuel consumption was 2.203 L/100 km, and this shows a 77.38% reduction in the fuel consumption. For the GA-PID control strategy (with optimal control gains of 70.6657, 0.3339, and 72.4406), the fuel consumption was 3.069 L/100 km, and the energy consumed by the battery and motor was 0.1295 kWh/km (12.95 kWh/100 km) and 0.1162 kWh/km (11.62 kWh/100 km). The power consumed by the battery and motor was 50.80 kW and 44.94 kW. The energy and power efficiencies are approximately equal, which were 89.73% and 88.46%, respectively. This is translated to the range extension of the Nissan Leaf battery pack from 128.75 km to 185.3281 km. Moreover, For the PSO-PI control strategy (with optimal control gains of 1243.1 and 1.3453), the energy consumed by the battery and motor was 0.1403 kWh/km (14.03 kWh/100 km) and 0.1228 kWh/km (12.28 kWh/100 km). The power consumed by the battery and motor was 55.06 kW and 48.61 kW. The energy and power efficiencies are approximately equal, at 87.53% and 88.29%, respectively. At the same time, the consumed battery and motor power for the FOPID strategy were 54.99 kW and 48.56 kW and energy consumption were 14 kWh/100 km and 12.28 kWh/100 km, respectively. Although all strategies show optimal consumption, it is evident that the proposed GA-PID strategy consumed less energy and power and gave wider km battery range. However, there was less energy loss in the case of GA-PID, which translated to better efficiency than the PSO-PI and FOPID control strategies.

Figure 36 shows the MAF and the engine at idle condition. In this condition, the vehicle was not moving (0 km/h); therefore, the engine operated at 819 rpm while the maximum speed was 1470 rpm to keep the fuel flowing. The MAF was 15.7644 g/s at this engine speed, and the MFF was 1.0872 g/s. The simulated fuel flow was 1.062 g/s when the simulated idle engine speed was 800 rpm. Moreover, Figure 35 shows the specified and actual boost pressures. The specified boost pressure, the actual boost pressure, and the engine speed are the interconnected parameters that affect the engine's performance. At 2310 rpm, the specified and actual boost pressures were 1.0275 bar and 1.1645 bar at 180 s, respectively. While the engine rpm increased to 2743 rpm, the turbocharger spun faster, generating more boost pressure, rising to 2.466 bar (actual boost). In this operating condition, it is observed that the actual boost pressure is greater than the specified boost pressure, which could lead to a potential decrease in engine efficiency and other damage. It is, therefore, crucial to monitor boost pressure and adjust the boost pressure regulator as needed to maintain the specified boost pressure. In addition, engine management could be developed to regulate the engine speed in the case of the simulated conventional Crafter to avoid potential damage due to the high rpm experienced in this research. In reality, diesel engines should not run at high rpm.

The experimental and simulated results presented in Figures 31–33 have been thoroughly analyzed in our previous paper [36], although there are slight differences due to the incorporation of meta-heuristics optimization. There is much more improvement in energy and fuel efficiency. However, Table 12 presents the fuel and energy consumption and the CO_2 according to the three control strategies and Table 13 presents the comparison between the conventional and hybrid powertrains fuel economy. For Table 12, it was observed that there was significant reduction in the fuel consumption in case of the all the control strategies with PSO-PI exhibiting better fuel economy. However, Table 13 presents the significant of the vehicle transformation with respect to the proposed control strategy. For the conventional Crafter, CO_2 of 255.4122 g/km has been emitted to the environment. The CO_2 emission was reduced to 74.79 g/km for the hybrid Crafter. According to the manufacturer datasheet, the CO_2 emissions of 223–232 g/km for the WLTP test procedure and 187–202 g/km for the new European derive cycle (NEDC) were achieved. Therefore, fewer emissions were achieved with the designed hybrid powertrain than with the conventional one.

The statistical analysis of the objective functions was performed using Wilcoxon signed rank test to justify the effectiveness of the proposed GA control strategy. Table 14 presents the values for the objective function computed based on the ITAE performance criteria for both the GA-PID and PSO-PI control algorithms. It was observed that the values for the objective functions at ITAE are higher than those obtained from others like IAE, ISE, approximately equal to 2.52944. This was the best value computed for the GA-PID. This shows how close to the stability the system was. The closer these values of the objective functions are to the zero, the more stable a system is. Still, it can be recommended that the proposed control algorithm be further enhanced to reach a more stable system. However, in some cases, improper tuning of the controller may force the controller to reduce the error but may not good for the system economically, especially in the case of electric vehicles under real test conditions. Therefore, using an optimizer to compute the controller's gains is highly recommended. Table 14 presents the statistical value for the objective function for the GA-PID and PSO-PI controllers.

Table 14. Statistical Analysis of the Objective Function using Wilcoxon Signed Rank Test.

S/N	GA-PID	PSO-PI	Difference	Ranks	Signed Ranks
1	18.50	136.24	−117.74	7	−7
2	18.13	113.48	−95.35	6	−6
3	18.63	94.77	−76.14	5	−5
4	31.04	86.19	−55.15	2	−2
5	18.37	85.37	−67	4	−4
6	19.02	83.44	−64.42	3	−3
7	31.48	83.33	−51.85	1	−1

We use a non-parametric approach (Wilcoxon signed rank test), assuming that the statistical data is not normally distributed and the research hypothesis is one-sided. If W is the Wilcoxon ranks, W^+ is the sum of the positive ranks, and W^- is the sum of the negative ranks. Therefore, $W^+ = 0$ and $W^- = 7+6+5+2+4+3+1 = 28$. Therefore, the test statistics, W is:

$$W = min(W^+, W^-) = min(28, 0) = 0 \tag{28}$$

The critical value of W should be obtained from the table if it supports the null hypothesis (H_0) or research hypothesis (H_1). From the table, $W = 4$ for sample size, $n = 7$ at a level of significance ($\alpha = 0.05$). The sample size of $n = 7$ was chosen because that was the last 7 datasets of the objective functions for the PSO-PI to start getting stabilized. Therefore, the condition is that we reject H_0 if $W \leq 4$. Therefore, the research hypothesis is true since $0 \leq 4$. This shows that there was a significant increase in the objective functions from the GA to PSO strategies, which is undesirable in our case. Similarly, the results showed that GA-PID had less power and energy consumption and higher power and energy efficiency than PSO-PI and FOPID strategies. The FOPID was found to be challenging during the tuning process due to the higher number of parameters and real implementation would be difficult for our application. Although GA-PID had higher fuel consumption, it outperformed the other methods when considering all the reference performance indicators.

7. Conclusions

This article has presented a successful transformation of the VW Crafter from conventional to plug-in hybrid for the first time on the basis of GA-PID for optimized system efficiency and reduced CO_2 emissions. The effectiveness of the proposed control strategy was verified by the PSO-PI and FOPID controllers. This transformation advances the understanding of the significance of hybrid technology compared to their counterpart, electric vehicles, which are characterized by limited range and high cost. The VW Crafter in this research was designed based on the 2.0 TDI diesel engine. The 2.0 TDI is characterized by its higher output torque, reduced consumption, and lower emission than the 2.5 L TDI engine, which had turbo failure although redesigned in 2010. The engine cooperated with a 2011 Nissan Leaf battery pack having 24 kWh rated capacity and capable of producing outpower of over 90 kW. With GA-PID, the fuel consumption was reduced from 9.739 L/100 km to 3.069 L/100 km, and energy efficiency was approximately 90%. It outperforms the PSO-PI and FOPID in terms of the optimized system energy and power efficiency as well as the battery range.

The control strategy was applied to meet the needs of optimized system efficiency robustness and reduce the cost of real implementation, considering the parametric uncertainty, external disturbances and intricate nonlinearities present in the system. The proposed controller has demontrated a robust performance regarding optimal fuel consumption and reduced emissions. Moreover, the successful transition of the VW Crafter from a conventional to a hybrid with efficient performance proved that the proposed control algorithm is realistic and, therefore, serves as a suitable alternative strategy for optimal consumption and reduced emissions in the field of electric and hybrid vehicles. For future development, although this research is not aimed at optimizing a traditional powertrain, engine management is necessary for the conventional Crafter to keep the engine operating at the appropriate speed. Moreover, the integration of GA and PSO techniques can be proposed to optimize the powertrain further to realize a more stable state of the system. At the same time, the actual boost pressure should be adequately regulated to maintain optimal fuel flow to the combustion chamber for the efficient performance of the conventional Crafter.

Author Contributions: Conceptualization, A.B. and P.T.S.; methodology, A.B. and P.T.S.; software, A.B.; validation, A.B. and P.T.S.; formal analysis, A.B.; investigation, A.B.; resources, P.T.S.; data curation, A.B. and P.T.S.; writing—original draft preparation, A.B.; writing—review and editing, P.T.S.; visualization, A.B.; supervision, P.T.S.; project administration, P.T.S.; funding acquisition, P.T.S. All authors have read and agreed to the published version of the manuscript.

Funding: This research was funded by the TKP2020-NKA-04 project implemented with support from Hungary's National Research, Development, and Innovation Fund, financed under the 2020-4.1.1-TKP2020 funding scheme. The authors wish to thank the Hungarian Research Fund (OTKA K143595). The authors wish to acknowledge the University of Debrecen for its financial support.

Data Availability Statement: The data presented in this research are available on request from the authors.

Acknowledgments: Aminu Babangida wishes to acknowledge Aliko Dangote University of Science and Technology,Wudil (formerly known as Kano University of Science and Technology,Wudil) for its moral, spiritual, and financial support. The authors wish to acknowledge Diós Szabolcs Sándor, our departmental engineer for the assistance in this project.

Conflicts of Interest: The authors declare no conflicts of interest.

References

1. Yang, C.; Zhou, H.; Chen, X.; Huang, J. Demand Time Series Prediction of Stacked Long Short-Term Memory Electric Vehicle Charging Stations Based on Fused Attention Mechanism. *Energies* **2024**, *17*, 2041. [CrossRef]
2. Liu, Y.; Chen, M.; Fan, Y.; Ying, L.; Cui, X.; Zou, X. Design of a Stochastic Electricity Market Mechanism with a High Proportion of Renewable Energy. *Energies* **2024**, *17*, 3044. [CrossRef]
3. Kim, G. Electric Vehicle Routing Problem with States of Charging Stations. *Sustainability* **2024**, *16*, 3439. [CrossRef]
4. Yan, Y.-H.; Leou, R.-C.; Ko, C.-C. A Model for Electrifying Fire Ambulance Service Stations Considering Practical Service Data and Charging Strategies. *Energies* **2024**, *17*, 1445. [CrossRef]
5. Menyhart, J. Overview of Sustainable Mobility: The Role of Electric Vehicles in Energy Communities. *World Electr. Veh. J.* **2024**, *15*, 275. [CrossRef]
6. Santos, J.B.; Francisco, A.M.B.; Cabrita, C.; Monteiro, J.; Pacheco, A.; Cardoso, P.J.S. Development and Implementation of a Smart Charging System for Electric Vehicles Based on the ISO 15118 Standard. *Energies* **2024**, *17*, 3045. [CrossRef]
7. Zhang, Q.; Tian, S. Energy Consumption Prediction and Control Algorithm for Hybrid Electric Vehicles Based on an Equivalent Minimum Fuel Consumption Model. *Sustainability* **2023**, *15*, 9394. [CrossRef]
8. Xu, D.; Zheng, C.; Cui, Y.; Fu, S.; Kim, N.; Cha, S.W. Recent progress in learning algorithms applied in energy management of hybrid vehicles: A comprehensive review. *Int. J. Precis. Eng. Manuf.-Green Technol.* **2023**, *10*, 245–267. [CrossRef]
9. Romero, C.A.; Correa, P.; Ariza Echeverri, E.A.; Vergara, D. Strategies for Reducing Automobile Fuel Consumption. *Appl. Sci.* **2024**, *14*, 910. [CrossRef]
10. Ahmed, A.; Amit T.; Swastik P. Modeling and optimization of HEV for FTP driving cycle. *AIP Conf. Proc.* **2024**, *2962*, 020047.
11. Peng, F.; Ye Z.; Guohua S.; Jianchang H.; Zhiqiang Z.; Lei Y. Evaluation of Real-World Fuel Consumption of Hybrid-Electric Passenger Car Based on Speed-Specific Vehicle Power Distributions. *J. Adv. Transp.* **2023**, *1*, 9016510. [CrossRef]
12. Jui, J.J.; Mohd, A.A.; Imran, M.M.M.; Muhammad, I.M.R. Optimal Energy Management Strategies for Hybrid Electric Vehicles: A Recent Survey of Machine Learning Approaches. *J. Eng. Res.* **2024**, *in press*. [CrossRef]
13. Cao, Y.; Yao, M.; Sun, X. An Overview of Modelling and Energy Management Strategies for Hybrid Electric Vehicles. *Appl. Sci.* **2023**, *13*, 5947. [CrossRef]
14. Tie, S.F.; Chee W.T. A review of energy sources and energy management system in electric vehicles. *Renew. Sustain. Energy Rev.* **2013**, *20*, 82–102. [CrossRef]
15. Du, A.; Chen, Y.; Zhang, D.; Han, Y. Multi-Objective Energy Management Strategy Based on PSO Optimization for Power-Split Hybrid Electric Vehicles. *Energies* **2021**, *14*, 2438. [CrossRef]
16. González-Romera, E.; Romero-Cadaval, E.; Roncero-Clemente, C.; Milanés-Montero, M.-I.; Barrero-González, F.; Alvi, A.-A. A Genetic Algorithm for Residential Virtual Power Plants with Electric Vehicle Management Providing Ancillary Services. *Electronics* **2023**, *12*, 3717. [CrossRef]
17. Wang, Y.; Jiao, X. Dual Heuristic Dynamic Programming Based Energy Management Control for Hybrid Electric Vehicles. *Energies* **2022**, *15*, 3235. [CrossRef]
18. Liu, Y.; Sun, Q.; Liu, C.; Han, Q.; Guo, H.; Han, W. Fuel consumption optimization for a plug-in hybrid electric bus during the vehicle-following scenario. *J. Energy Storage* **2023**, *64*, 107187. [CrossRef]
19. Adedeji, B.P. A multivariable output neural network approach for simulation of plug-in hybrid electric vehicle fuel consumption. *Green Energy Intell. Transp. 2* **2023**, *2*, 100070. [CrossRef]
20. Mortabit, I.; Aziz, R.; Nidale, E.; Seddik, K.; Elhoussaine, S.; Abdelilah, E.; Hassan, E. Instantaneous Vehicle Fuel Consumption Estimation Using Neural Networks. In *Proceeding of the International Symposium on Automatic Control and Emerging Technologies*; Springer Nature: Singapore, 2023; pp. 702–713. [CrossRef]
21. Maaruf, M.; Hamanah, W.M.; Abido, M.A. Hybrid Backstepping Control of a Quadrotor Using a Radial Basis Function Neural Network. *Mathematics* **2023**, *11*, 991. [CrossRef]
22. Abd-Elhaleem, S.; Walaa S.; Abdel A.S. Improved Power Management Under Uncertain Driving Conditions for Plug-In Hybrid Electric Vehicles via Intelligent Controller. *IEEE Trans. Intell. Transp. Syst.* **2023**, *24*, 13698–13712. [CrossRef]
23. Wang, H.; Ziba A.; Yiming Y.; Jiangfeng Z.; Bin X. FlexNet: A warm start method for deep reinforcement learning in hybrid electric vehicle energy management applications. *Energy* **2024**, *288*, 129773. [CrossRef]
24. Gao, H.; Xuanming Z.; Xiaohua Z.; Dongpo Y.; Dafeng S.; Lanqi Z. Predictive cruise control for hybrid electric vehicles based on hierarchical convex optimization. *Energy Convers. Manag.* **2024**, *299*, 117883. [CrossRef]
25. Ibrar, A.; Sohaira A.; Ayla S.; Nazo H. Efficiency enhancement strategy implementation in hybrid electric vehicles using sliding mode control. *Electr. Eng. Electromech.* **2023**, *1*, 10–19. [CrossRef]
26. Ghazali, A.K.; Norazlina A.A. Supertwisting sliding mode control for parallel hybrid electric vehicle control strategy. In Proceeeding of the 2023 IEEE 13th Symposium on Computer Applications and Industrial Electronics (ISCAIE), Penang, Malaysia, 20–21 May 2023; pp. 283–286. [CrossRef]
27. Yao, Z.; Yoon, H.-S.; Hong, Y.-K. Control of Hybrid Electric Vehicle Powertrain Using Offline-Online Hybrid Reinforcement Learning. *Energies* **2023**, *16*, 652. [CrossRef]
28. Rajasekar, V.; Bragadeshwaran A. Improvised energy management control through neuro-fuzzy based adaptive ECMS approach for an optimal battery utilization in non-plugin parallel hybrid electric vehicle. *Proc. Inst. Mech. Eng. Part C J. Mech. Eng. Sci.* **2024**, *238*, 3308–3326. [CrossRef]

29. Katona, K.; Neamah, H.A.; Korondi, P. Obstacle Avoidance and Path Planning Methods for Autonomous Navigation of Mobile Robot. *Sensors* **2024**, *24*, 3573. [CrossRef]
30. Szántó, A.; Hajdu, S.; Sziki, G.Á. Optimizing Parameters for an Electrical Car Employing Vehicle Dynamics Simulation Program. *Appl. Sci.* **2023**, *13*, 8897. [CrossRef]
31. Xu, L.; Wang, Y.; Li, Y.; Zhao, J.; Liu, M. Research on Control Strategy of APSO-Optimized Fuzzy PID for Series Hybrid Tractors. *World Electr. Veh. J.* **2023**, *14*, 258. [CrossRef]
32. Nassef, A.M.; Abdelkareem, M.A.; Maghrabie, H.M.; Baroutaji, A. Metaheuristic-Based Algorithms for Optimizing Fractional-Order Controllers—A Recent, Systematic, and Comprehensive Review. *Fractal Fract.* **2023**, *7*, 553. [CrossRef]
33. Suid, M.H.; Mohd, A.A. Optimal tuning of sigmoid PID controller using Nonlinear Sine Cosine Algorithm for the Automatic Voltage Regulator system. *Isa Trans.* **2022**, *128*, 265–286. [CrossRef] [PubMed]
34. Ghazali, M.R.; Ahmad, M.A.; RMT Raja, I. Data-driven neuroendocrine-PID controller design for twin rotor MIMO system. *J. Phys. Conf. Ser.* **2020**, *529*, 042080. [CrossRef]
35. Babangida, A.; Korondi, P.; Sándor, S.D.; Szemes, P.T. Development of Meta-Heuristic Optimization Based Control of Redesigned VW Crafter Hybrid Vehicle. In Proceeding of the 2024 IEEE 21st Power Electronics and Motion Conference (PEMC 2024), Pilsen, Czech Republic, 30 September–3 October 2024.
36. Babangida, A.; Light Odazie, C.M.; Szemes, P.T. Optimal Control Design and Online Controller-Area-Network Bus Data Analysis for a Light Commercial Hybrid Electric Vehicle. *Mathematics* **2023**, *11*, 3436. [CrossRef]
37. Srinivasan, C. Energy management of hybrid energy storage system in electric vehicle based on hybrid SCSO-RERNN approach. *J. Energy Storage* **2024**, *78*, 109733. [CrossRef]
38. Zheng, Y.; Yunhong C.; Xiaosong H.; Xin S.; Daniel-Ioan S.; Remus T. Thermal state monitoring of lithium-ion batteries: Progress, challenges, and opportunities. *Prog. Energy Combust. Sci.* **2024**, *100*, 101120. [CrossRef]
39. Hayes, J.G.; Goodarzi, G.A. 2011 Nissan Battery Pack. In *Electric powertrain: Energy Systems, Power Electronics and Drives for Hybrid, Electric and Fuel Cell Vehicles*; John Wiley and Sons Ltd.: West Sussex, UK, 2018.
40. Norbakyah, J.S.; Daniel, H.W.C.; Atiq, W.H.; Daud, M.Z.; Salisa, A.R. Modeling, simulation and model optimization of internal combustion engine for PHERB powertrain. *Jurnal Teknologi* **2017**, *79*, 161–173. [CrossRef]
41. Generic Internal Combustion Engine-Matlab. Available online: https://www.mathworks.com/help/sdl/ref/genericengine.html (accessed on 5 January 2024).
42. Ahssan, M.R.; Ektesabi, M.; Gorji, S. Gear Ratio Optimization along with a Novel Gearshift Scheduling Strategy for a Two-Speed Transmission System in Electric Vehicle. *Energies* **2020**, *13*, 5073. [CrossRef]
43. Oglieve, C.J.; Mohammadpour, M.; Rahnejat, H. Optimisation of the vehicle transmission and the gear-shifting strategy for the minimum fuel consumption and the minimum nitrogen oxide emissions. *Proc. Inst. Mech. Eng. Part D J. Automob. Eng.* **2017**, *231*, 883–899. [CrossRef]
44. Virani, V.; Swapnil A.; Jaydeepsinh B. Modelling and Control of PMSM Drive by Field Oriented Control For HEV. C, Modelling and Control of PMSM Drive by Field Oriented Control For HEV (February 12, 2019). Advances in Power Generation from Renewable Energy Sources (APGRES) 2019. Available online: https://papers.ssrn.com/sol3/papers.cfm?abstract_id=3442515 (accessed on 10 January 2021).
45. Bodzás, S.; Zsolt T.; Piroska A.; Géza H. Redesign of a Volkswagen Crafter vehicle to a hybrid vehicle having e-motor and diesel engine. *IOP Conf. Ser. Mater. Sci. Eng.* **2022**, *1237*, 012008. [CrossRef]
46. Kortenbruck, G.; Jakubczyk, L.; Nowak, D.F. Voltage Signals Measured Directly at the Battery and via On-Board Diagnostics: A Comparison. *Vehicles* **2023**, *5*, 637–655. [CrossRef]
47. Valeika, G.; Matijošius, J.; Orynycz, O.; Rimkus, A.; Kilikevičius, A.; Tucki, K. Compression Ignition Internal Combustion Engine's Energy Parameter Research Using Variable (HVO) Biodiesel and Biobutanol Fuel Blends. *Energies* **2024**, *17*, 262. [CrossRef]
48. Merkle, L.; Pöthig, M.; Schmid, F. Estimate e-Golf Battery State Using Diagnostic Data and a Digital Twin. *Batteries* **2021**, *7*, 15. [CrossRef]
49. Anton, B.; Adriana, F. Design and development of series-hybrid automotive powertrains. *IEEE Access* **2020**, *8*, 226026–226041. [CrossRef]
50. Eltayeb, A.; Ahmed, G.; Imran, I.H.; Alyazidi, N.M.; Abubaker, A. Comparative Analysis: Fractional PID vs. PID Controllers for Robotic Arm Using Genetic Algorithm Optimization. *Automation* **2024**, *5*, 230–245. [CrossRef]
51. Noordin, A.; Mohd Basri, M.A.; Mohamed, Z. Adaptive PID Control via Sliding Mode for Position Tracking of Quadrotor MAV: Simulation and Real-Time Experiment Evaluation. *Aerospace* **2023**, *10*, 512. [CrossRef]
52. Noordin, A.; Basri, M.A.M.; Mohamed, Z. Simulation and Experimental Study on Pid Control of a Quadrotor MAV with Perturbation. *Bull. Electr. Eng. Inform.* **2020**, *9*, 1811–1818. [CrossRef]
53. Abdel-hamed, A.M.; Abdelaziz, A.Y.; El-Shahat, A. Design of a 2DOF-PID Control Scheme for Frequency/Power Regulation in a Two-Area Power System Using Dragonfly Algorithm with Integral-Based Weighted Goal Objective. *Energies* **2023**, *16*, 486. [CrossRef]
54. Qu, Z.; Younis, W.; Wang, Y.; Georgievitch, P.M. A Multi-Source Power System's Load Frequency Control Utilizing Particle Swarm Optimization. *Energies* **2024**, *17*, 517. [CrossRef]
55. Gaya, M.S.; Auwal M.; Abdulkadir, R.A.; Salim, S.N.S.; Madugu, I.S.; Tijjani, A.; Yusuf, L.A.; Umar, I.D.; Khairi, M.T.M. Enhanced pid vs model predictive control applied to bldc motor. *IOP Conf. Ser. Mater. Sci. Eng.* **2018**, *303*, 012017. [CrossRef]

56. Kroičs, K.; Būmanis, A. BLDC Motor Speed Control with Digital Adaptive PID-Fuzzy Controller and Reduced Harmonic Content. *Energies* **2024**, *17*, 1311. [CrossRef]
57. Ma, C.; Huang, B.; Basher, M.K.; Rob, M.A.; Jiang, Y. Fuzzy PID Control Design of Mining Electric Locomotive Based on Permanent Magnet Synchronous Motor. *Electronics* **2024**, *13*, 1855. [CrossRef]
58. Qu, S.; He, T.; Zhu, G. Model-Assisted Online Optimization of Gain-Scheduled PID Control Using NSGA-II Iterative Genetic Algorithm. *Appl. Sci.* **2023**, *13*, 6444. [CrossRef]
59. Mohamed, N.A.; Hasanien, H.M.; Alkuhayli, A.; Akmaral, T.; Jurado, F.; Badr, A.O. Hybrid Particle Swarm and Gravitational Search Algorithm-Based Optimal Fractional Order PID Control Scheme for Performance Enhancement of Offshore Wind Farms. *Sustainability* **2023**, *15*, 11912. [CrossRef]
60. Sun, X.; Liu, N.; Shen, R.; Wang, K.; Zhao, Z.; Sheng, X. Nonlinear PID Controller Parameters Optimization Using Improved Particle Swarm Optimization Algorithm for the CNC System. *Appl. Sci.* **2022**, *12*, 10269. [CrossRef]
61. Chen, J.; Lu, Q.; Bai, J.; Xu, X.; Yao, Y.; Fang, W. A Temperature Control Method for Microaccelerometer Chips Based on Genetic Algorithm and Fuzzy PID Control. *Micromachines* **2021**, *12*, 1511. [CrossRef]
62. Precup, R.; Preitl S.; Korondi P. Fuzzy controllers with maximum sensitivity for servosystems. *IEEE Trans. Ind. Electron.* **2007**, *54*, 1298–1310. [CrossRef]
63. Nishat, M.M.; Faisal, F.; Evan, A.J.; Rahaman, M.M.; Sifat, M.S.; Rabbi, H.M.F. Development of Genetic Algorithm (GA) Based Optimized PID Controller for Stability Analysis of DC-DC Buck Converter. *J. Power Energy Eng.* **2020**, *8*, 8–19. [CrossRef]
64. Moreno-Suarez, L.E.; Morales-Velazquez, L.; Jaen-Cuellar, A.Y.; Osornio-Rios, R.A. Hardware-in-the-Loop Scheme of Linear Controllers Tuned through Genetic Algorithms for BLDC Motor Used in Electric Scooter under Variable Operation Conditions. *Machines* **2023**, *11*, 663. https:// doi.org/10.3390/machines11060663. [CrossRef]
65. Yakut, Y.B. A new control algorithm for increasing efficiency of PEM fuel cells–Based boost converter using PI controller with PSO method. *Int. J. Hydrogen Energy* **2024**, *75*, 1–11. [CrossRef]
66. Magdy, G.G.; Shabib, A.A.; Elbaset, T.K.; Yaser, Q.; Hassan, B.; Yasunori, M. Tustin's technique based digital decentralized load frequency control in a realistic multi power system considering wind farms and communications delays. *Ain Shams Eng. J.* **2019**, *10*, 327–341. [CrossRef]
67. Wang, P.; Chen, X.; Zhang, Y.; Zhang, L.; Huang, Y. Fractional-Order Load Frequency Control of an Interconnected Power System with a Hydrogen Energy-Storage Unit. *Fractal Fract.* **2024**, *8*, 126. [CrossRef]
68. Github.com. Available online: https://github.com/maybachy1121/Simscape-Powertrain-SI-Model (accessed on 10 December 2023).
69. Maaruf, M.; Khan, K.; Khalid, M. Robust Control for Optimized Islanded and Grid-Connected Operation of Solar/Wind/Battery Hybrid Energy. *Sustainability* **2022**, *14*, 5673. [CrossRef]
70. Parczewski, K.; Wnęk, H. Analysis of Energy Flow in Hybrid and Electric-Drive Vehicles. *Energies* **2024**, *17*, 1915. [CrossRef]
71. Meseguer, J.E.; Carlos T.C.; Juan C.C.; Pietro M. Assessing the impact of driving behavior on instantaneous fuel consumption. In Proceedings of the 2015 12th annual IEEE Consumer Communications and Networking Conference (CCNC), Las Vegas, NV, USA, 9–12 January 2015; pp. 443–448.
72. Rimpas, D.A.P.; Maria S. OBD-II sensor diagnostics for monitoring vehicle operation and consumption. *Energy Rep.* **2020**, *6*, 55–63. [CrossRef]
73. Balcı, Ö.; Karagöz, Y.; Gezer, O.; Kale, S.; Köten, H.; Pusat, S.; Yüksek, L. Numerical and experimental investigation of fuel consumption and CO_2 emission performance for a parallel hybrid vehicle. *Alex. Eng. J.* **2021**, *60*, 3649–3667. [CrossRef]